The deacylase SIRT5 supports melanoma viability by regulating chromatin dynamics

William Giblin[1,2], Lauren Bringman-Rodenbarger[1], Surinder Kumar[1], Mary E. Skinner[1], Angela Guo[1], Ahmed M. Mostafa[1,3], Michelle Azar[1], Ahmed S.A. Mady[1], Carolina H. Chung[4], Namrata Kadambi[1], Keith-Allen Melong[1], Ho-Joon Lee[4], Li Zhang[5], Peter Sajjakulnukit[5], Sophie Trefely[6,7], Erika L. Varner[7], Sowmya Iyer[8], Min Wang[1], James S. Wilmott[9], H. Peter Soyer[10,11], Richard A. Sturm[10], Antonia L. Pritchard[12,13], Aleodor Andea[1,14], Richard A. Scolyer[9,15], Mitchell S. Stark[10], David A. Scott[16], Douglas R. Fullen[1,14], Marcus W. Bosenberg[17], Sriram Chandrasekaran[4,18,19,20], Zaneta Nikolovska-Coleska[1,20], Monique Verhaegen[14], Nathaniel W. Snyder[7], Miguel N. Rivera[8,21], Andrei L. Osterman[16], Costas Lyssiotis[5,20,22], and David B. Lombard[1,20,23*]

[1]Department of Pathology, University of Michigan, Ann Arbor, MI 48109 USA

[2]Department of Human Genetics, University of Michigan, Ann Arbor, MI 48109 USA

[3]Department of Biochemistry, Faculty of Pharmacy, Ain Shams University, Cairo, Egypt

[4]Department of Biomedical Engineering, University of Michigan, Ann Arbor, MI 48109 USA

[5]Department of Molecular and Integrative Physiology, University of Michigan, Ann Arbor, MI 48109 USA

[6]Department of Cancer Biology, University of Pennsylvania, Perelman School of Medicine, Philadelphia, PA 19104 USA

[7]Center for Metabolic Disease Research, Department of Microbiology and Immunology, Temple University, Lewis Katz School of Medicine, Philadelphia, PA 19140 USA

[8]Department of Pathology and MGH Cancer Center, Massachusetts General Hospital and Harvard Medical School, Boston, MA 02115 USA

[9]Melanoma Institute Australia and Sydney Medical School, The University of Sydney, Sydney, New South Wales, 2006 Australia

[10]The University of Queensland Diamantina Institute, The University of Queensland, Dermatology Research Centre, Brisbane, QLD 4102 Australia

[11]Department of Dermatology, Princess Alexandra Hospital, Brisbane, Queensland 4102 Australia

[12]Institute of Health Research and Innovation, University of the Highlands and Islands, An Lóchran, 10 Inverness Campus, Inverness, IV2 5NA United Kingdom

[13]Oncogenomics, QIMR Berghofer Medical Research Institute, Brisbane, Queensland, 4006 Australia

[14]Department of Dermatology, University of Michigan, Ann Arbor, MI 48109 USA

[15]Tissue Pathology and Diagnostic Oncology, Royal Prince Alfred Hospital, and New South Wales Health Pathology, Sydney, New South Wales, 2050 Australia

[16]Sanford Burnham Prebys Medical Discovery Institute, La Jolla, California 92037 USA

[17]Departments of Pathology and Dermatology, Yale University School of Medicine, New Haven, CT 06510 USA

[18]Program in Chemical Biology, University of Michigan, Ann Arbor, MI 48109 USA

[19]Center for Computational Medicine and Bioinformatics, University of Michigan, Ann Arbor, MI 48109 USA

[20]Rogel Cancer Center, University of Michigan Medical School, Ann Arbor, MI 48109 USA

[21]Broad Institute of Harvard and MIT, Cambridge, MA 02142 USA

[22]Division of Gastroenterology, Department of Internal Medicine, University of Michigan, Ann Arbor, MI 48109 USA

[23]Institute of Gerontology, University of Michigan, Ann Arbor, MI 48109 USA

*Correspondence:

University of Michigan

3015 BSRB

109 Zina Pitcher Place

Ann Arbor, MI 48109

(734) 615-0498

davidlom@med.umich.edu

Conflict of interest:

MWB is a consultant for Eli Lilly and Company. RAS reports receiving fees for professional services from Merck Sharp & Dohme, GlaxoSmithKline Australia, Bristol-Myers Squibb, Dermpedia, Novartis Pharmaceuticals Australia Pty Ltd, Myriad, NeraCare GmbH and Amgen. CAL is an inventor on patents pertaining to KRAS regulated metabolic pathways, redox control pathways in pancreatic cancer, and targeting GOT1 as a therapeutic approach. CAL is also an author on a provisional patent application concerning the development of technologies that integrate the metabolic flux assay with cellular high content image analysis. DBL reports ownership of the equivalent in voting stock or share of ABBV and GILD.

Abstract

Cutaneous melanoma remains the most lethal skin cancer, and ranks third among all malignancies in terms of years of life lost. Despite the advent of immune checkpoint and targeted therapies, only roughly half of patients with advanced melanoma achieve a durable remission. SIRT5 is a member of the sirtuin family of protein deacylases that regulate metabolism and other biological processes. Germline *Sirt5* deficiency is associated with mild phenotypes in mice. Here we show that SIRT5 is required for proliferation and survival across all cutaneous melanoma genotypes tested, as well as uveal melanoma, a genetically distinct melanoma subtype that arises in the eye, and is incurable once metastatic. Likewise, SIRT5 is required for efficient tumor formation by melanoma xenografts, and in an autochthonous mouse *Braf;Pten*-driven melanoma model. Via metabolite and transcriptomic analyses, we find that SIRT5 is required to maintain histone acetylation and methylation levels in melanoma cells, thereby promoting proper gene expression. SIRT5-dependent genes notably include *MITF*, a key lineage-specific survival oncogene in melanoma, and the *c-MYC* proto-oncogene. SIRT5 may represent a novel, druggable genotype-independent addiction in melanoma.

Introduction

Cutaneous melanoma remains the most lethal skin cancer. In 2019, there were an estimated 96,480 new melanoma cases and 7,230 melanoma-related deaths in the US. Melanoma incidence is rising (1), and melanoma ranks third among all cancers in terms of years of life lost (2, 3). Despite the advent of immune checkpoint and targeted therapies, only about half of patients with advanced melanoma achieves long-term remission, even with optimal immune checkpoint therapy (4). Uveal melanoma represents a genetically and clinically distinct subtype of melanoma that arises in the eye, and currently has no effective treatment options once metastatic (5). New therapeutic strategies for advanced melanoma are desperately needed.

Mammalian sirtuins are a family of seven NAD^+-dependent lysine deacylases that regulate diverse processes to promote cellular and organismal homeostasis and stress responses. Among these proteins, Sirtuin 5 (SIRT5) has remained a somewhat enigmatic and poorly characterized sirtuin. SIRT5 is atypical, in that it lacks robust deacetylase activity, and primarily functions to remove succinyl, malonyl, and glutaryl modifications from lysines on its target proteins, in mitochondria and throughout the cell, thereby regulating multiple metabolic pathways (6-13).

SIRT5-deficient mice are viable, fertile, and mostly healthy (14, 15), with the most prominent effects described to date occurring in the myocardium (16). *Sirt5* knockout (KO) mice are more susceptible to ischemia-reperfusion injury and exhibit impaired recovery of cardiac function compared to wild type (WT) mice (17). Aged *Sirt5* KO mice develop cardiac hypertrophy and mildly impaired ejection fraction (18). Whole-body *Sirt5* KOs, but not cardiomyocyte-specific KOs, show increased lethality in response to cardiac pressure overload (19, 20). Overall, the lack of strong phenotypes associated with SIRT5 loss-of-function in normal tissues has hindered

progress in understanding the biological significance of SIRT5 and its target post-translational modifications.

Multiple sirtuins are now linked to neoplasia, as tumor suppressors and/or oncogenes, in a context-specific manner (21). The functions of SIRT5 in cancer are incompletely understood, and a subject of active investigation (6). For example, SIRT5 promotes chemoresistance in non-small cell lung carcinoma cells by enhancing NRF2 activity and expression of its targets involved in cellular antioxidant defense (22). SIRT5 promotes Warburg-type metabolism in lung cancer cells by negatively regulating SUN2, a member of the linker of nucleoskeleton and cytoskeleton complex (23). SIRT5 suppresses levels of reactive oxygen species (ROS) via desuccinylation of multiple targets (superoxide dismutase 1, glucose-6-phosphate dehydrogenase, and isocitrate dehydrogenase (IDH) 2), thereby promoting growth of lung cancer cell lines *in vitro* (24, 25). SIRT5 also plays an important role in facilitating tumor cell growth by desuccinylating serine hydroxymethyltransferase 2 (SHMT2), which catalyzes the reversible, rate-limiting step in serine catabolism, providing methyl groups for cellular methylation reactions via one-carbon metabolism (1CM) (26). Another study indicated that SIRT5 promotes hepatocellular carcinoma (HCC) proliferation and invasion by targeting the transcription factor E2F1 (27). Similarly, it was recently reported that SIRT5 suppresses apoptosis by deacetylation of cytochrome C, thereby promoting HCC growth (28). SIRT5 also promotes breast cancer tumorigenesis by desuccinylating and stabilizing glutaminase (29), an enzyme that catalyzes the conversion of glutamine to glutamate, which supports the metabolic demands of tumorigenesis (30). In contrast, SIRT5 opposes malignant phenotypes associated with expression of mutant IDH, which generates the novel oncometabolite R-2-hydroxyglutarate, thereby perturbing the epigenome (31). IDH mutant glioma cells show increased protein succinylation, exhibit mitochondrial dysfunction and are resistant to apoptosis. Ectopically

expressed SIRT5 in these cells impaired their growth *in vitro* and *in vivo*. Another recent report indicates that SIRT5 inactivates STAT3, thus suppressing mitochondrial pyruvate metabolism in lung cancer (32).

Here, we identify a critical requirement for SIRT5 in melanoma cell survival, through chromatin regulation. In all cutaneous and uveal melanoma cell lines tested, from both humans and mice and with varied genetic drivers, SIRT5 depletion resulted in rapid loss of proliferative capacity and cell death. Likewise, SIRT5 loss reduced melanoma formation in xenograft and autochthonous mouse melanoma models. Via transcriptomic analysis, we identified a core set of genes that responds to SIRT5 depletion. Among these, *MITF*, an essential lineage-specific transcription factor in melanoma, is downregulated, along with expression of its targets (33). SIRT5 loss is also associated with reduced expression of *c-MYC*, a well-described proto-oncogene that is often overexpressed in metastatic melanoma and melanoma cell lines (34). We link the effects of SIRT5 depletion on gene expression to alterations in histone methylation and acetylation induced by metabolic changes occurring in the context of SIRT5 loss-of-function. Taken together, our results identify SIRT5 as a novel genotype-independent dependency in melanoma cells, likely exerting its effects via chromatin modifications zand gene regulation. Given the modest effects of SIRT5 loss-of-function in normal tissues, SIRT5 may represent an attractive therapeutic target in melanoma and potentially other cancer types.

Results

The chromosomal region encompassing *SIRT5* shows frequent copy number gain in human melanoma

In humans, the *SIRT5* gene localizes to chromosome 6p23. The 6p region exhibits frequent copy number gain in melanoma, an event associated with an adverse prognosis, both in melanoma (35) and other cancers (36). To confirm that gain of the *SIRT5* locus specifically occurs in human melanomas, we mined TCGA data (37) using cBioportal, and observed that copy number gain or amplification of *SIRT5* was present in 55% of melanoma cases, whereas *SIRT5* deletion or mutation was rare (Figure 1A, S1A, and S1B). Increased *SIRT5* copy number also correlated with increased *SIRT5* mRNA expression in these samples (Figure S1C). In contrast, the presence of extra copies of the other six sirtuins was comparatively rare in melanoma (Figure 1A and S1A). Activating mutations in *NRAS* and *BRAF* represent the most common oncogenic drivers in cutaneous melanoma (38). *SIRT5* gain or amplification was observed in melanomas with either driver, and in melanomas with the less common driver mutation, *NF1* (Figure 1A). Increased *SIRT5* copy number was associated with moderately worsened overall survival (p=0.0097; Figure 1B), although not progression-free survival (Figure S1D).

To assess further the status of the *SIRT5* locus in melanoma, we performed fluorescence in situ hybridization (FISH) analysis of *SIRT5* and the centromere of chromosome 6 in an independent group of melanoma samples (Figure 1C and S1E). Consistent with TCGA data, increased *SIRT5* copy number was observed in 38% (12/32) of cases analyzed overall, with co-amplification of *SIRT5* and the centromere of chromosome 6 present in 16% (5/32) of cases. Similarly, using comparative genomic hybridization analysis in yet another independent group of melanoma samples, gain of the *SIRT5* locus was present in 27% of melanoma cases analyzed (37/139), the most frequent gain among any of the sirtuins (Figure 1D).

We then interrogated *SIRT5* mRNA expression in melanomas of varied depth of invasion, and found that increased *SIRT5* mRNA expression occurred in melanomas of greater Clark's level, which are more clinically aggressive and confer a worse prognosis (39, 40) (Figure 1E). Similarly, we examined SIRT5 protein expression in tissue microarrays containing examples of benign and dysplastic nevi, as well as localized and metastatic melanomas. We found by immunohistochemistry that SIRT5 protein was overexpressed in melanomas relative to benign melanocytic lesions (Figure 1F).

To begin to characterize the stage of melanogenesis at which *SIRT5* gain occurs, we screened a panel of genomically characterized benign and dysplastic nevi (n=30) (41) for *SIRT5* somatic mutations and copy number aberrations. No deleterious point mutations were identified in *SIRT5*; however, there was evidence of regional loss of heterozygosity encompassing the *SIRT5* locus in 3/30 benign nevi (10%) assayed (Table S1). However, no *SIRT5* copy number gain or amplification was identified in any of the nevus samples, supporting the idea that *SIRT5* amplification represents a relatively late event in melanomagenesis. This is consistent with the known rarity of such genomic events in nevi (41, 42). Overall, these data show that gain or amplification of *SIRT5* is a common genomic event in melanoma but not nevi.

SIRT5 is required for survival of BRAF^{V600E} and NRAS^{Q61R} melanoma cells

We assessed the potential requirement of SIRT5 in melanoma cells using a panel of 10 *BRAF or NRAS* mutant melanoma cell lines (Table S2). SIRT5 protein was readily detectable by immunoblot in all cell lines tested (Figure S2A). We initially depleted *SIRT5* using two lentiviral shRNAs targeting distinct regions of the *SIRT5* mRNA (knockdown (KD) 1 and KD2) (10). Although predominantly mitochondrial, SIRT5 is also present in the cytosol and the nucleus (10), and was efficiently depleted from all of these compartments upon *SIRT5* shRNA

transduction in all cell lines tested (Figure S2B and S2C). In both $NRAS^{Q61R}$ and $BRAF^{V600E}$ cells, SIRT5 depletion induced rapid loss of proliferation over the course of 7 days (Figure 2A and S2D). Similar results were obtained in an *in vitro* colony forming assay (Figure 2B). Vemurafenib is a targeted therapy FDA-approved for treatment of BRAF-mutant melanoma. Patients treated with targeted therapies often rapidly relapse with drug-resistant disease (43). SIRT5 inhibition in a vemurafenib-resistant derivative of the melanoma cell line SK-MEL-239, SK-MEL-239**VR**, induced rapid loss of proliferation upon SIRT5 KD, indicating that these vemurafenib-resistant cells retained SIRT5 dependency (Figure 2A and S2E). To complement shRNA-based studies, and to further evaluate the requirement of melanoma cells for SIRT5, we mutated the *SIRT5* locus via CRISPR-Cas9, using four distinct guide RNAs (gRNAs, G1-G4) targeting SIRT5. A dramatic reduction in colony formation was observed in *SIRT5* mutant populations compared to control (Figure 2C). Thus, genetic ablation of *SIRT5* dramatically reduces melanoma cell growth, consistent with results obtained using shRNA-mediated SIRT5 depletion.

Loss of SIRT5 leads to apoptotic cell death in cutaneous and uveal melanoma cells

We evaluated the mechanism of cellular attrition induced by SIRT5 loss-of-function. SIRT5 depletion in melanoma cells induced cleavage of caspase 3 (Figure 3A and 3B) and induction of Annexin V positivity (Figure 3C and 3D). Importantly, SIRT5 depletion also blocked proliferation and induced cleavage of caspase 3 in uveal melanoma cell lines (Figure 3B; top panel; representative of 4/4 uveal melanoma cell lines tested; see Table S2). Cell loss and induction of caspase 3 cleavage at 96 hrs. post-transduction were also observed, to varying degrees, with an additional 3 unique shRNAs targeting human SIRT5 (Figure 3B; middle panel), and 5 unique shRNAs targeting murine SIRT5 in YUMM5.2, a mouse melanoma cell line (44) (Figure 3B; bottom panel). Thus, SIRT5 is required for survival and proliferation of multiple genetically

diverse melanoma cell lines *in vitro*, in both human and mouse, and for survival of human uveal melanoma cells.

SIRT5 supports robust melanoma tumor formation *in vivo*

To investigate the potential requirement for SIRT5 to support melanoma tumor development *in vivo*, we initially employed a xenograft assay. Immediately following transduction with SIRT5 shRNAs, A2058 melanoma cells were subcutaneously injected into the flanks of female NOD/SCID mice (Figure S3A); tumor growth was followed by serial measurement of tumor volume (Figure 4A; left panel). SIRT5 depletion greatly impaired tumor growth and reduced tumor size at endpoint relative to controls (Figure 4A; right panel, 4B and S3B).

To examine the role of SIRT5 in melanoma development in a more physiologic, immunocompetent context, we crossed *Sirt5* KO mice to a commonly-used mouse melanoma model, the *Braf*^{CA}*;Pten*$^{fl/fl}$*;Tyr::CreER* strain (45). Topical application of 4-hydroxytamoxifen (4HT) in this system induces activated BRAF expression and ablation of *Pten* in melanocytes, resulting in melanoma development. In males, SIRT5-deficient mice showed an approximately 3-fold reduction in tumor mass on average (WT: 1.005±0.618g vs. KO: 0.323±0.198g, $p<0.05$, (Figure 4C and 4D). In our colony, female mice showed rapid ulceration of even small melanoma tumors following induction, requiring euthanasia of the host and rendering it difficult to assess the effects of SIRT5 in melanoma in females. Thus, SIRT5 promotes human and mouse melanoma growth, both in cell culture and *in vivo*.

Neither glucose nor glutamine metabolism are greatly altered by SIRT5 loss

Initially, we considered the possibility that SIRT5 depletion might induce global metabolic collapse and energetic catastrophe in melanoma. SIRT5 has been reported to promote mitochondrial respiration (46, 47) and glycolysis (13). We previously showed that SIRT5

suppresses mitochondrial respiration through Pyruvate Dehydrogenase and Complex II in 293T cells and liver mitochondria (10), a finding recapitulated in some systems (32), but not others (46, 47). We used the XFe96 Extracellular Flux Analyzer to assess the effects of SIRT5 depletion on cellular bioenergetics in melanoma cells. Relative to SIRT5-proficient controls, SIRT5 KD A2058 or A375 cells did not show consistent changes in the extracellular acidification rate (ECAR), a measure of cellular glycolysis (Figure 5A). Likewise, glucose-dependent mitochondrial oxygen consumption rate (OCR), ATP production, and mitochondrial membrane potential were not consistently affected by SIRT5 depletion (Figure 5B-5D).

Melanoma and many other cancer types replenish the TCA cycle in part via glutaminolysis (48-51). In this pathway, glutaminase (GLS) catalyzes conversion of glutamine to glutamate, generating carbon and nitrogen to fuel the metabolic demands of tumorigenesis. In breast cancer cells, SIRT5 desuccinylates GLS to protect it from ubiquitination and subsequent degradation. Loss of SIRT5 resulted in decreased GLS expression, exogenous glutamine consumption, glutamine-derived intracellular metabolite levels, and cellular proliferation (29). These findings, along with reports that inhibiting glycolysis or glutamine metabolism sensitizes melanoma cells to cell death, prompted us to investigate a potential role for SIRT5 in promoting glutamine metabolism in melanoma (52, 53). We cultured control or SIRT5 KD A2058 cells in medium containing glutamine labeled with stable isotopes ([$^{15}N_2$]-glutamine or [$^{13}C_5$]-glutamine) or in medium containing [$^{13}C_6$]-glucose, and measured both labeling derived from ^{13}C or ^{15}N and total quantities of cellular metabolites. Following SIRT5 KD, the fractional labeling of glutamine derived metabolites (glutamate, aspartate and TCA cycle metabolites) decreased when cultured with [$^{13}C_5$]-glutamine, but showed corresponding (or compensatory) increases in labeling when cultured with $^{3}C_6$-glucose (Figure S4A-S4B). Labeling derived from $^{15}N_2$-glutamine decreased in one KD A2058 cell line but not the other (Figure S4C). Overall, these results provide evidence consistent with previous results showing that SIRT5 promotes glutaminase activity (29).

However, importantly, total cellular amounts of glutamate, aspartate, TCA cycle or other metabolites were not consistently reduced by SIRT5 loss (Figure S4D), indicating that although the depletion of SIRT5 may reduce glutaminase activity, this effect is insufficient to compromise levels of essential cellular metabolites. In parallel studies, glutamine-dependent mitochondrial OCR, and GLS protein levels, were assessed, and were not appreciably altered by SIRT5 depletion across multiple melanoma cell lines (Figure S4E and S4F). Moreover, incubation of SIRT5 KD A2058 cells with exogenous non-essential amino acids plus alpha-ketoglutarate – interventions that can rescue defects in glutamine catabolism (51) – in the context of SIRT5 KD failed to rescue the proliferative defect observed upon SIRT5 loss (Figure S4G). Taken together, these data indicate that neither glycolysis nor glutamine metabolism represent major SIRT5 target pathways in promoting melanoma viability.

Transcriptomic analysis reveals a requirement for SIRT5 in supporting *MITF* and *MITF* target gene expression

To understand the requirement of melanoma cells for SIRT5 mechanistically, RNA-seq based transcriptomic analysis was performed on three cutaneous melanoma cell lines (A2058, A375 and SK-MEL-2), each subjected to SIRT5 depletion using two distinct shRNAs (Table S3). A gene was scored as differentially expressed only if it was consistently altered in all technical replicates by both independent SIRT5 shRNAs. We identified core sets of genes whose expression responded to SIRT5 KD, many of which overlapped among the cell lines (Figure 6A and 6B). Among SIRT5-responsive genes was the Melanocyte Inducing Transcription Factor (*MITF*), a key lineage-specific oncogenic transcription factor in melanoma that plays crucial roles in development and proliferation of melanocytes (33). MITF is expressed in human melanomas, and *MITF* amplification, present in a subset of melanoma tumors, portends a poor prognosis (54). In cutaneous melanoma cells with robust baseline MITF expression, MITF protein and mRNA expression declined markedly in response to SIRT5 KD (Figure 6C and 6D),

associated with decreased expression of MITF's canonical targets: genes involved in metabolism (*PPARGC1A*), melanocytic differentiation (*TYR*, *MLANA*), cell survival (*BCL2*) and others (Figure 6D). A trend towards a reduced *MITF* gene expression profile was also observed in A375 cells upon SIRT5 KD (Figure S5A). Likewise, decreased *SIRT5*, *MITF* and *MITF* target gene expression was validated by qRT-PCR in A2058 cells, and to a lesser degree, in SK-MEL-2 (Figure S5B). We also observed a decrease in MITF protein levels upon SIRT5 KD in MP-41 cells, a uveal melanoma line (Figure 6C).

To assess the potential relationship between SIRT5 and MITF in a more physiologic, non-loss-of-function setting, we mined TCGA data, to test whether any correlation exists between *SIRT5* and *MITF* mRNA expression in melanoma clinical samples. Consistent with the RNA-seq data, mRNA co-expression analysis revealed a strong positive correlation between *SIRT5*, *MITF* and two canonical *MITF* target genes, *PPARGC1A* and *BCL2*. Indeed, the correlation between *SIRT5* and *MITF* expression was stronger than that of *MITF* with these two targets (Figure 6E and S5C). As a specificity control, *SIRT3* levels showed a modest, negative correlation with *MITF* expression (Figure S5C). These data suggest that SIRT5 expression levels influence expression of *MITF* and its targets in patient melanoma tumors.

Previous reports demonstrate that the proto-oncogene *c-MYC* is upregulated in melanoma tumors and cell lines, acting to bypass mutant BRAF- or NRAS-induced senescence during melanomagenesis (34). Furthermore, siRNA KD of c-MYC in melanocytic tumor cells results in a loss of MITF expression (55). Consistent with these data, we observed a loss of MITF expression and a concomitant reduction in expression of *c-MYC* in SIRT5-depleted melanoma cell lines. Both c-*MYC* RNA and c-MYC protein levels were decreased in melanoma cells after SIRT5 ablation (Figure S5D and S5E). A positive correlation between *SIRT5* and *c-MYC* RNA expression in melanoma tumors from TCGA data was observed (Figure S5C). Taken together,

these data show that SIRT5 promotes expression of two key oncogenic drivers, MITF and c-MYC, in melanoma.

SIRT5 regulates melanoma cell metabolism to promote histone acetylation

To obtain systems-level insight into potential roles for SIRT5 in regulating metabolism and gene expression, we re-analyzed our transcriptomic data, using a genome-scale model of human metabolism to identify metabolic reactions that change in activity after SIRT5 KD. The Recon1 human network model used contains a relationship between 3,744 reactions, 2,766 metabolites,1,496 metabolic genes, and 2,004 metabolic enzymes (56). This network model has been used successfully to predict the metabolic behavior of various cancer cells and stem cells (57, 58). Using this model, we identified a metabolic flux state most consistent with expression data for each of the three cell lines after SIRT5 depletion. This was achieved by maximizing the activity of reactions that are associated with up-regulated genes and minimizing flux through reactions that are down-regulated for each condition, while simultaneously satisfying the stoichiometric and thermodynamic constraints embedded in the model (see Methods).

The model identified 20 reactions among the 3744 that showed significantly different activity across all cell lines after SIRT5 KD ($p<0.01$; Figure 7A, Table S4). Among these, the enzyme ATP-Citrate Lyase (ACLY) was predicted to have the most significant change, with reduced activity after SIRT5 KD. ACLY generates acetyl-CoA from citrate, thereby playing an important role in supporting histone acetylation (59). Furthermore, the mitochondrial methylenetetrahydrofolate dehydrogenase reaction was also predicted to have reduced activity after SIRT5 loss, a part of the folate and one-carbon metabolism (1CM) pathways (see below). Several reactions involving cholesterol metabolism and nucleotide salvage were also affected by SIRT5 KD, highlighting the pervasive metabolic effects of SIRT5 in melanoma cells.

To test the predictions of the metabolic model, we evaluated protein acetylation levels in SIRT5 KD cells. Indeed, SIRT5 depletion induced a striking decrease in total lysine acetylation, most notably on histones, including H3K9 acetylation (H3K9ac) and H4K16 acetylation (H4K16ac) (Figure 7B and 7C). After 4 weeks in culture following SIRT5 KD, although SIRT5 depletion was maintained, a small residual population of SIRT5 KD A2058 cells overcame SIRT5 loss-of-function to survive and proliferate. Importantly, total lysine acetylation was restored in surviving SIRT5 KD A2058 cell populations after 4 weeks in culture (Figure 7D), consistent with the importance of maintaining histone acetylation levels in melanoma survival.

Protein acetyltransferases employ acetyl-CoA to acetylate their protein targets, including histones (60). To investigate the potential basis for reduced histone acetylation in SIRT5-depleted melanoma cells, we employed a sensitive mass spectrometry-based method to assess total cellular acetyl-CoA levels (61, 62). Surprisingly, we observed an *increase* of total cellular acetyl-CoA after SIRT5 KD (Figure 7E), implying that reduced acetyl-CoA levels may not contribute to the observed decrease in lysine acetylation upon SIRT5 depletion, and suggesting that reduced acetyltransferase activity may underlie the reduced acetylation levels in SIRT5-depleted melanoma cells (see Discussion).

SIRT5 promotes one-carbon metabolism and histone methylation in melanoma

To investigate further how SIRT5 may function to affect gene expression in melanoma, SIRT5-depleted melanoma cell lines were profiled using liquid chromatography coupled tandem mass spectrometry (LC-MS/MS)-based metabolomics, followed by functional analysis using MetaboAnalyst pathway enrichment (Table S5). Two *BRAF* mutant lines (A2058 and A375) and an *NRAS* mutant (SK-MEL-2) showed perturbations in pathways involving 1CM in response to SIRT5 depletion (Figure 8A, S6A and S6B). 1CM is comprised of the linked folate and methionine cycles (63). Outputs include metabolites required for amino acid and nucleotide

synthesis; glutathione for antioxidant defense; and crucially, S-adenosylmethionine (SAM) for methylation reactions, including those on histones. We observed a reduction in levels of several key 1CM metabolites upon SIRT5 depletion in *BRAF* mutant melanoma cell lines, but not in SK-MEL-2 (Figure 8B).

Histone methylation, particularly H3K4 trimethylation (H3K4me3), is highly sensitive to fluctuations in SAM levels (64). We observed reductions in H3K4me3 and H3K9me3 in melanoma cells following SIRT5 KD, consistent with 1CM perturbation (Figure 8C). However, addition of exogenous SAM did not consistently restore H3K4me3 or H3K9me3, nor did it markedly elevate levels of these marks in control cells (Figure S6C and not shown). Similar to acetylation, SIRT5-depleted melanoma cells that grew out after prolonged culture recovered H3K4me3 and H3K9me3 levels (Figure 8D), while maintaining reduced SIRT5 expression (Figure 7D), suggesting that loss of these histone modifications represents an important driver of the lethality associated with SIRT5 depletion in melanoma.

A decrease in cellular glutathione content occurring in the context of impaired 1CM would be predicted to elevate levels of cellular reactive oxygen species (ROS) (65). Consistently, in A2058 cells, we observed increased staining with 2′,7′-dichlorofluorescin diacetate (DCFDA), a ROS-sensitive dye, following SIRT5 depletion (Figure 8E). However, treatment with the antioxidants, N-acetylcysteine, mitoTEMPOL or β-mercaptoethanol failed to mitigate cell lethality after SIRT5 loss (data not shown), indicating that regulation of ROS levels is not likely a primary determinant of the requirement of melanoma cells for SIRT5.

A previously identified SIRT5 substrate, SHMT2, is a mitochondrial enzyme that converts serine and tetrahydrofolate to glycine and 5,10-methylene tetrahydrofolate, in turn providing methyl groups for 1CM (26). SIRT5 desuccinylates SHMT2, thereby promoting its activity and

proliferation of cancer cells (26). We also noted that previous proteomic surveys identified the 1CM enzyme, MTHFD1L (methylenetetrahydrofolate dehydrogenase ($NADP^+$ dependent) 1 like), as another candidate SIRT5 substrate (10, 66). MTHFD1L is a 1CM enzyme that participates in the folate cycle to convert formate and tetrahydrofolate into 10-formyl-tetrahydrofolate in an ATP-dependent reaction. We tested the interaction of MTHFD1L with SIRT5 in the context of melanoma, and found that MTHFD1L co-immunoprecipitates with SIRT5 (Figure 8F). These data suggest a potential role for SIRT5 in regulating multiple 1CM enzymes, such as SHMT2 and potentially MTHFD1L and others, to promote 1CM and histone methylation. Likewise, since SK-MEL-2 cells showed a reduction in histone H3K4me3 levels without apparent declines in 1C metabolites under our experimental conditions, it is likely that SIRT5 plays additional roles in regulating histone methylation, perhaps in an oncogenic driver-dependent manner. We hypothesize that SIRT5 regulates histone methylation and acetylation via regulation of multiple protein targets in melanoma cells.

Discussion

Sirtuin-family NAD^+-dependent protein deacylases regulate metabolism and other diverse aspects of cell biology (67). SIRT5 is a poorly-understood, atypical sirtuin, whose primary known biochemical function is to remove succinyl, malonyl, and glutaryl groups from lysines on its target proteins (7, 8, 10-12). A substantial fraction of SIRT5 is present in the mitochondrial matrix; however SIRT5 is present and functional in the cytosol, and even in the nucleus (10, 13). Most of the phenotypes associated with SIRT5 loss-of-function in normal cells and tissues reported in the literature to date are remarkably mild (16). In sharp contrast, here we report that cutaneous and uveal melanoma cells show exquisite dependency on SIRT5, in a genotype-independent manner. SIRT5 depletion, induced by shRNA or CRISPR/Cas9, provokes dramatic, rapid loss of cell viability and induction of apoptosis in both cutaneous and uveal melanoma cell lines. Likewise, SIRT5 promotes melanoma xenograft tumor formation in immunocompromised mice, and melanoma formation in an autochthonous *Braf*;*Pten*-driven mouse melanoma strain.

Our transcriptomic results reveal that SIRT5 plays a major role in maintaining proper gene expression in melanoma cells. SIRT5-dependent genes notably include the lineage-specific oncogenic transcription factor *MITF* (68) and *c-MYC* (34). In the TCGA dataset, *SIRT5* levels correlate with those of *MITF* and *c-MYC*, suggesting that SIRT5 activity influences both MITF and c-MYC expression in a physiologic context. Via metabolomic analysis, we identified a role for SIRT5 in promoting 1CM in two BRAF-dependent cell lines, and in maintaining histone trimethylation at H3K4 and H3K9, marks associated with transcriptional activation and repression, respectively. SIRT5 also plays a distinct role in maintaining histone acetylation. To our knowledge, SIRT5 is the first protein implicated in maintaining both histone methylation and

acetylation, highlighting its important roles in maintaining chromatin structure and gene expression in melanoma.

Our *in vivo* findings in an autochthonous system are in contrast to a recently published study by Moon *et al.,* in which SIRT5 deficiency was found to exert no impact on tumor growth in a similar mouse melanoma model as the one used in our studies (69). Several potential explanations exist for this discrepancy. Moon *et al.* used a *Sirt5* allele distinct from the one employed in our work; the *Sirt5* allele used in their analysis deletes a single exon in the *Sirt5* gene (15), whereas the one used herein deletes essentially the entire *Sirt5* protein coding sequence (14). Likewise, subtle genetic background differences in the strains of the mice used may contribute to these discrepancies, as could microbiome differences between the mouse colonies. Another potential explanation involves the protocol used to induce gene recombination; we applied a higher concentration of tamoxifen than did Moon *et al.* (64.5 mM versus 5 mM).

Transcriptomic analysis reveals that SIRT5 regulates expression of key genes involved in cell survival in melanoma, including *MITF* and its targets (54). MITF is a member of microphthalmia family of transcription factors, and is dysregulated in melanoma (70). Attenuation of melanocyte differentiation and pigmentation are observed in humans and mice deficient for MITF activity, highlighting the importance of MITF in melanocyte survival and function. Likewise, MITF is known to play key roles in melanoma cell survival and differentiation, and *MITF* amplification occurs in 15% to 20% of primary and metastatic melanomas, associated with a worsened prognosis (54). In melanoma cell lines where MITF is expressed, SIRT5 depletion induced a rapid decrease in expression of MITF and several well-characterized MITF targets. Likewise, in TCGA data, *SIRT5* and *MITF* levels were highly correlated, suggesting that SIRT5 may play a role in regulating MITF in tumors *in vivo*. Notably, we were unable to rescue the lethality of

SIRT5 depletion by overexpressing MITF in melanoma cells (data not shown); however, this experiment is complicated by the fact that MITF overexpression itself drives melanoma cells to leave the cell cycle and differentiate, and thus is likely selected against in short-term culture (71). Likewise, we were unable to rescue SIRT5-depleted melanoma cells via transduction with c-MYC-encoding lentiviruses (data not shown). Nevertheless, we hypothesize that loss of MITF and c-MYC expression likely represent important mechanisms through which SIRT5 promotes melanoma viability.

We did not observe major effects of SIRT5 depletion on OCR, ECAR, or overall ATP production in melanoma. Instead, through mass spectrometry-based metabolite profiling, we identified one-carbon metabolism (1CM) as a SIRT5 target pathway likely important for maintenance of gene expression and melanoma viability. 1CM consists of the linked folate and methionine cycles. A major output of 1CM is SAM, the universal methyl donor in mammalian cells. Metabolite profiling in *BRAF* mutant melanoma cells lacking SIRT5 reveals profound perturbations in levels of many 1C metabolites, including reductions in cellular SAM. Moreover, H3K4me3, a mark of active gene expression and a sensitive marker for intracellular SAM, drops in response to SIRT5 loss-of-function. Furthermore, global lysine acetylation and H3K9me3, which marks heterochromatic regions in the genome (72) decrease upon SIRT5 loss. Likewise, oxidative stress increases in SIRT5-depleted melanoma cells, consistent with impaired regeneration of reduced glutathione, a major antioxidant species and an output of 1CM.

Many questions remain as to the mechanisms by which SIRT5 promotes proper gene expression and viability in melanoma. The accumulation of acetyl-CoA in SIRT5-depleted melanoma cells suggests that SIRT5 may promote the activity of a histone acetyltransferase to promote histone acetylation, a possibility that we are currently investigating. Alternatively, SIRT5

could promote generation of a localized acetyl-CoA pool necessary to drive histone acetylation, without influencing global acetyl-CoA levels. In the context of 1CM, SIRT5 has previously been shown to desuccinylate and activate SHMT2, which converts serine to glycine, thereby providing one carbon units to 1CM (26). In addition, we identified MTHFD1L as another SIRT5 interactor and candidate target which could also plausibly play a role in SIRT5-mediated regulation of 1CM. Unfortunately, we have been unsuccessful at rescuing the cellular lethality associated with SIRT5 depletion using relevant small molecule metabolites or drugs (acetate, acetyl-CoA, SAM, serine, glycine, histone deacetylase and demethylase inhibitors, antioxidants, and amino acids [data not shown]). We suspect that this reflects pleiotropic functions and targets of SIRT5 in melanoma cells, impairment of which cannot be rescued by intervention in any individual pathway. SIRT5 targets involved in other pathways -- *e.g.* ROS suppression, cell death (26, 73), and others -- could well contribute to the requirement of melanoma cells for SIRT5. This is consistent with the hundreds of cellular targets of SIRT5, involved in diverse cellular pathways, identified in proteomics studies (16). Moreover, it is consistent with the observation that SIRT5 plays pro-survival roles across multiple different cancer types, via distinct proposed mechanisms. As the dominant cellular desuccinylase/demalonylase/deglutarylase, it is possible that SIRT5 is recruited to play distinct roles in supporting tumorigenesis, modulating activities of different suites of targets and pathways, in a cancer type-specific manner.

Overall, our data reveal a major, hitherto unknown requirement for SIRT5 in melanoma cell survival, through suppression of apoptosis via regulation chromatin modifications and expression of critical pro-survival genes, including MITF and c-MYC (Figure 8G). These results, along with those already in the literature (6), suggest that SIRT5 may play potent oncogenic roles across many diverse tumor types, seemingly engaging a variety of different cellular

mechanisms to do so in a cancer- and context-specific manner. Since the phenotypes of *Sirt5* null mice are quite mild, we propose that SIRT5 may represent an attractive new therapeutic target, in melanoma and specific other cancer types. In this regard, published studies (16) demonstrate that SIRT5 is in principle druggable with small molecules. SIRT5 dependency may be particularly therapeutically significant in uveal melanoma, where currently no effective therapeutic options exist for patients with metastatic disease.

Materials and Methods

Analysis of SIRT5 gene amplification, mRNA and protein expression in melanoma

Percentages of genetic alterations, as indicated, in *SIRT1-SIRT5*, *BRAF*, *NRAS*, *PTEN*, *MITF* and *NF1* in human melanoma cases were calculated from TCGA data (n=287, Provisional, analyzed on cBioPortal). Kaplan–Meier analysis of overall or disease-free survival in melanoma patients with or without copy number gain or amplification of *SIRT5* were similarly analyzed. Sirtuin copy number analysis of melanoma cell lines was performed by high density SNP array of 8 primary, 72 stage III, 51 stage IV and 8 stage III/IV (metastatic disease) melanoma cell lines, as previously described (39, 40). Data were analyzed using Nexus Copy Number (BioDiscovery) for copy gain, copy loss and loss of heterozygosity of genes and chromosomal regions. Data from the TCGA was used via cBioPortal to further investigate *SIRT5* in melanoma (n=478; Cancer Genome Atlas Network), including copy number (by GISTIC 2.0) and expression data (by RNAseq) and correlation with clinical attributes, including the Clark level at diagnosis of the melanoma.

Immunohistochemical analysis of SIRT5 in human nevus and melanoma

The study was undertaken with Human Ethics Review Committee approval and patient's informed consent. The Melanoma Institute Australia Medical Research Database and archival files of the Department of Tissue Pathology and Diagnostic Oncology, Royal Prince Alfred Hospital, were utilized to identify melanocytic lesions (human ethics committee approval X11-0289, HREC/11/RPAH/444). Melanocytic lesions were selected based on the pathological diagnosis of the melanocytic lesion as a compound nevus, dysplastic nevus, thin primary melanoma (Breslow thickness <1mm), thick primary melanoma (Breslow thickness >1mm) or metastatic melanoma in regional lymph node or distant metastatic site. Immunohistochemical SIRT5 staining intensity in melanocytes was scored by two pathologists blinded as to the diagnosis associated with each tissue core. Scores were then averaged.

Cell culture

Cutaneous melanoma cell lines with mutations in either *NRAS* or *BRAF*: A375, A2058, SK-MEL-2, SK-MEL-28, VMM15, and VMM917 were purchased from ATCC (Table S2); SK-MEL-19 was generously provided by Monique Verhaegen (UM); C8161 was provided by Dr. Zaneta Nikolovska-Coleska (UM); SK-MEL-239 and vemurafenib-resistant (SK-MEL-239**VR)** lines were generously provided by Dr. Emily Bernstein (ISMMS). Uveal melanoma cell lines MP-38, MP-41 and MP-46 were purchased from ATCC; cell line 92-1 was purchased from Sigma-Aldrich (Table S2). HEK293T cells were purchased from ATCC.

Unless otherwise noted, A375, A2058, SK-MEL-19 and 293T cell lines were cultured in DMEM (Gibco) containing 4.5g/L glucose, 110mg/L sodium pyruvate, 4mM L-glutamine, 100units/mL penicillin, 100µg/mL streptomycin and 10% heat-inactivated FBS. SK-MEL-2 and SK-MEL-28 cell lines were cultured in MEM (Gibco) containing 1.0g/L glucose, 110mg/L sodium pyruvate, 2mM L-glutamine, 0.1mM non-essential amino acids (Gibco), 100units/mL penicillin, 100µg/mL streptomycin solution and 10% heat-inactivated FBS. VMM15, VMM917, SK-MEL-239 and SK-MEL-239**VR** cell lines were cultured in RPMI (Gibco) containing 4.5g/L glucose, 10mM HEPES, 110mg/L sodium pyruvate, 4mM L-glutamine, 100units/mL penicillin, 100µg/mL streptomycin and 10% heat-inactivated FBS. SK-MEL-239**VR** derivative cells were cultured in 2µM vemurafenib (Cayman Chemical). The C8161 cell line was grown in DMEM/F12 (1:1) (Gibco) containing 1.2mM L-glutamine, 0.1mM non-essential amino acids, 100units/mL penicillin, 100µg/mL streptomycin and 5% heat-inactivated FBS. MP-38, MP-41 and MP-46 cells were cultured in RPMI (Gibco) containing 2 mM L-glutamine, 10 mM HEPES, 110mg/L sodium pyruvate, 4.5g/L glucose, 100units/mL penicillin, 100µg/mL streptomycin and 25% heat-inactivated FBS; 92-1 cells were cultured in RPMI (Gibco) containing 2 mM L-glutamine, 10 mM HEPES, 110mg/L sodium pyruvate, 4.5g/L glucose, 100units/mL penicillin, 100µg/mL streptomycin and 10% heat-inactivated FBS. S-adenosylmethionine (SAM) resuspended in

0.005M sulfuric acid and 10% ethanol was purchased from New England Biolabs. All cell lines were routinely confirmed to be free of mycoplasma contamination by PCR assay and were grown in a humidified chamber at 37°C containing 5% CO_2. All cutaneous melanoma and 293T cell lines were authenticated via STR profiling at the University of Michigan DNA Sequencing Core (data available upon request). Table S2 lists the genetic alteration of each cell line, and the sex and age of the patient at the time of cell line derivation, if known.

Lentiviral transduction

Lentiviral plasmids in the pLKO.1 backbone, encoding puromycin *N*-acetyl-transferase, containing shRNAs targeting human *SIRT5* or murine *Sirt5* (Table S6) were used to generate high-titer lentiviral particles at the Vector Core (UM). A non-silencing control shRNA against Gaussia luciferase was used as the non-targeting control (NT). KD3 and KD4 shRNA lentiviral plasmids targeting human *SIRT5* were designed based on previously published CRISPR screens (74, 75). All other shRNA plasmids were purchased through the Vector Core (UM). Lentiviral transduction was carried out in the presence of 8 μg/ml polybrene in complete growth medium for 24 hrs., after which medium was replaced with fresh complete growth medium. Puromycin was added to a final concentration of 1 μg/ml 48 hrs. post-transduction to select for transductants. Successful SIRT5 KD was routinely confirmed by western blotting 48-96 hrs. post-transduction.

Proliferation assays

Forty-eight hrs. after lentiviral transduction, $5x10^3$ cells were plated into 96-well plates in the presence of 1μg/ml puromycin or in 1μg/ml puromycin with a cocktail of 0.1mM non-essential amino acids (Gibco) and 5mM alpha-ketoglutarate (Sigma), where indicated. Twenty-four hrs. after plating, relative cell mass was assessed using WST-1 Cell Proliferation Reagent (Clontech) per manufacturer's instruction. After addition of WST-1, plates were incubated at

37ºC for 2 hrs. before reading the optical density at 450nm. OD450nm was assessed every 24 hrs. as indicated and plotted.

Colony formation assays

Two million A2058 or SK-MEL-2 melanoma cell lines were lentivirally transduced in a 10-cm dish with a non-silencing shRNA or one of two shRNAs targeting human *SIRT5*. Forty-eight hrs. post-transduction $1x10^5$ cells were plated into each of four wells of a six-well dish as previously described. Twelve days after transduction, puromycin-selected cells were stained with 0.25% (w/v) crystal violet (Sigma) in 20% ethanol for 30 minutes according to standard protocols. Colony formation was quantified by solubilizing crystal violet in a 30% methanol, 10% acetic acid solution and absorbance measured at OD590nm.

CRISPR/Cas9 targeting of SIRT5

CRISPR plasmids were generated as described (76). Briefly, guide sequences (Table S6) targeting the *SIRT5* locus were inserted into pSpCas9(BB)-2A-Puro (PX459) backbone (Addgene catalog #62988). Guide sequences were designed based on previous CRISPR screens (74, 75, 77). Sanger sequencing confirmed successful cloning of guide sequences. A2058 cells were seeded at 50,000 cells/well two days prior to transfecting 500ng of each indicated plasmid using polyethylenimine (PEI) in DMEM without serum or antibiotics. Transfected cells were selected using puromycin (1 µg/ml) for 7 days, beginning 24 hrs. post-transfection. Fourteen days after transfection, cells were fixed and stained with 0.25% crystal violet in 20% ethanol for 30 mins at room temperature. Colony formation was quantified by solubilizing crystal violet in a 30% methanol, 10% acetic acid solution and absorbance measured at OD590nm. Confirmation of SIRT5 KD via immunoblot was performed 33 days post-transfection.

Immunoblotting

Whole-cell protein extracts were prepared in protein sample buffer (62.5mM Tris pH 6.8, 2% SDS, 10% glycerol). Lysates were sonicated for 30 seconds using a Branson Sonifier set to output "2." Lysates were then clarified by centrifugation at 15,000rcf for 30 minutes at 4ºC. Protein concentrations were determined using DC Protein Assay (Bio-Rad). Equivalent amounts (10-50 µg) of total protein, supplemented with 710mM β-mercaptoethanol and 0.01% (w/v) bromophenol blue, then boiled for 5 minutes, were fractionated by SDS-PAGE on a 12% or 15% polyacrylamide gel, electrophoretically transferred to PVDF, and probed with antibodies diluted in 5% nonfat milk in 1XTBS-0.1% Tween-20. Membranes were imaged on an ImageQuant LAS 4000 Scanner (GE Healthcare) after application of Immobilon Western HRP Substrate (Millipore). See Table S7 for antibodies used in this study.

Immunofluorescence

A2058 cells were plated at a density of $0.5x10^6$ per well in six-well plates containing glass coverslips (Werner #1.5 thickness, 12mm diameter). Twenty-four hrs. later, cells were transduced with either a lentivirus expressing a non-silencing shRNA (control) or one of two shRNAs targeting *SIRT5* (KD1 or KD2). Ninety-six hrs. after transduction, puromycin-selected cells were incubated with 100nM Mitotracker (BD Biosciences) for 30 minutes at 37ºC, washed with PBS, and fixed in 3.7% formaldehyde. After permeabilization in 0.3% Triton X-100 for 10 minutes at room temperature, cells were blocked with 5% normal goat serum in 0.2% Triton X-100 in PBS for one hour. Cells were incubated in SIRT5 (Sigma) primary antibody diluted to 1 µg/ml in 5% bovine serum albumin in 0.2% Triton X-100 in PBS overnight at 4ºC. Cells were then washed 3 times in 1X PBS and incubated in Alexa 488 anti-rabbit (Invitrogen) diluted 1:1000 in 5% bovine serum albumin in 0.2% Triton X-100 in PBS for 1 hour at room temperature. Cells were washed 2 times in 1X PBS, and 1X with PBS supplemented with 0.01

μg/ml DAPI. Cells were mounted with prolong gold antifade reagent (ThermoFisher) and imaged on an Olympus FV 500 Confocal microscope.

Annexin V flow cytometry

A2058 and SK-MEL-2 cells were plated at a density of $0.5x10^6$ per well of two six-well plates/cell line. Four wells of each cell line were transduced with either a lentivirus expressing a non-silencing shRNA (control) or one of two shRNAs targeting *SIRT5* (KD1 or KD2). Ninety-six hrs. after transduction, puromycin-unselected cells were harvested and stained for 30 minutes at room temperature with FITC Annexin V (BD Biosciences) and propidium iodide (Sigma), according to the BD Biosciences staining protocol. Cells were analyzed by flow cytometry using a BD FACSCalibur and results were plotted using FlowJo 10.2 analysis software.

Xenograft assays

A2058 puromycin-unselected cells were harvested 72 hrs. post-transduction with pLKO control, pLKO *SIRT5* KD1, or pLKO *SIRT5* KD2. Subcutaneous tumor growth was initiated by injection of $1x10^6$ cells of each cell line, resuspended in 1:1 DMEM:Matrigel Matrix (Corning), into the contralateral flanks of 11-13 week old NOD.Cg-*Prkdc*^{scid}*Hr*^{hr}/NCrHsd female mice (Envigo). Each experimental group contained 5 mice. Tumor size was measured in millimeters (mm) using Vernier calipers at the timepoints indicated. Tumor volume was calculated according to the formula:

$$V = \frac{X(Y^2)}{2}$$

where V is tumor volume in mm^3, X is the longest length of the tumor, and Y is the shortest length of the tumor, perpendicular to X (78, 79). All mice were euthanized when a tumor ulcerated or reached $2000mm^3$. All mice were housed at the Biomedical Science Research

Building (UM). All vertebrate animal experiments were approved by and performed in accordance with the regulations of the University Committee on Use and Care of Animals.

Tumor induction in $Braf^{CA}$;$Pten^{fl/fl}$;Tyr::CreER;Sirt5 mice

Sirt5 KO mice (14) were crossed with *$Braf^{CA}$;$Pten^{fl/fl}$;Tyr::CreER* mice (45) to generate groups of littermate *$Braf^{CA}$;$Pten^{fl/fl}$;Tyr::CreER;Sirt5* KO and WT controls on a mixed BL/6/129SvJ genetic background. For melanoma induction, flanks of adult mice (4-9 weeks of age) were treated with depilatory cream with a cotton applicator. After 3-5 minutes, the area was rinsed with distilled water, and the treatment spot marked. Topical administration of 4-hydroxytamoxifen (4-HT; 25mg/ml in DMSO, Cayman Chemical) was repeated on each of three consecutive days, by applying one microliter of 4-HT to the spot. Mice were monitored for tumor appearance, which occurred typically within 4-8 weeks, and euthanized when a tumor ulcerated or reached 2000mm^3. All mice were housed at the Biomedical Science Research Building (UM). Experiments were approved by and performed in accordance with the regulations of the University Committee on Use and Care of Animals.

Transcriptomic analysis of SIRT5 depletion

A2058, A375 and SK-MEL-2 cells were plated at a density of 0.5x10^6/well of two six-well plates per cell line. Four wells of each cell line were transduced with either a lentivirus expressing a non-silencing shRNA (control) or one of two shRNAs targeting *SIRT5* (KD1 or KD2). Total RNA was extracted in TRIzol (Invitrogen) 96 hrs. post-transduction from three wells and treated with RNAse-free DNAse I (Roche) for 1 hour at 37ºC, according to manufacturer's instructions. RNA samples (n=3 biological replicates for each of 3 cell lines for each condition) were submitted to the University of Michigan Sequencing Core for sample processing and Illumina HiSeq-4000 50nt paired-end sequencing. The remaining well was harvested for protein to confirm SIRT5 KD

by immunoblot. Illumina libraries were prepared using random primers according to manufacturer's instructions.

Reads were aligned to hg19 using STAR (80). Mapped reads were filtered to exclude PCR duplicates and reads mapping to known ribosomal RNA coordinates, obtained from the repeat masker (rmsk) table in the UCSC database (http://genome.ucsc.edu). Gene expression was calculated using featureCounts (81). Only primary alignments with mapping quality of 10 or more were counted. Counts were then normalized to 1 million reads. Signal tracks were generated using bedtools (82). Differential expression was calculated using DESeq2 (83). DEseq analysis of gene expression changes, comparing control to changes common to both KDs, was used to generate the Venn diagrams in Figure 6A. Calculated p-values, after adjusting for multiple comparisons, < 0.05 were considered significant.

Identifying differentially active reactions using genome-scale metabolic modeling

Gene expression data from the melanoma cell lines A2058, A375, and SK-MEL-2 was used as input to identify differentially active reactions in the human genome-scale metabolic model using a modeling approach detailed in Shen *et al.* (84, 85). This approach identifies a metabolic flux state that best fits the transcriptomics profile in each condition. Normalized expression data for each cell line was compared between the two groups (C vs. KD) to attain a list of significantly up- and down-regulated genes using a significance threshold of $p<0.05$ and a z-score threshold above 2 or below -2, respectively. These genes were then overlaid onto the metabolic model based on gene-protein-reaction annotations in the model. Finally, reaction flux data was generated using a linear optimization version of the iMAT algorithm (58, 85) with the following inputs: the RECON1 model, the list of up- and down-regulated genes, and the recommended values for the optional parameters (rho = 1E-1, kappa = 1E-1, epsilon = 1, mode = 0). This resulted in flux predictions for all three cell lines. Differentially active reactions were identified by

transforming the fluxes into z-scores and estimating the significance of the difference between z-scores before and after KD across all cell lines using a t-test. The flux data for all the reactions is available in Table S4. Flux data was visualized through heatmaps generated using R software, where reactions were clustered by rank correlation. Only reactions with significant flux difference between control and KD groups ($p<0.01$) are shown. Transport reactions were excluded from the analysis.

Acetyl-CoA Quantification

Acetyl-CoA were quantified by stable isotope dilution liquid chromatography-high resolution mass spectrometry, as previously described (61, 62). Cell pellets were spiked with an internal standard prepared as described (61), and sonicated for 12 cycles of 0.5 sec. pulses in 10% (w/v) trichloroacetic acid (Sigma Aldrich) in water. Protein was pelleted by centrifugation at 17,000rcf for 10 min. at 4ºC. The cleared supernatant was purified by solid-phase extraction using Oasis HLB 1cc (30 mg) SPE columns (Waters). Columns were washed with 1ml methanol, equilibrated with 1ml water, loaded with sample, desalted with 1ml water, and eluted with 1ml methanol containing 25 mM ammonium acetate. The purified extracts were evaporated to dryness under nitrogen and resuspended in 55µl 5% (w/v) 5-sulfosalicylic acid (SSA) in optima HPLC grade water. Acetyl-CoA was measured by liquid chromatography-high resolution mass spectrometry. Briefly, 5µl of sample in 5% SSA were analyzed by injection into an Ultimate 3000 HPLC coupled to a Q Exactive Plus (Thermo Scientific) mass spectrometer in positive ESI mode using the settings described previously (62). Calibration curves were prepared using analytical standards from Sigma Aldrich and processed identically as the samples. Data were integrated using Tracefinder v4.1 (Thermo Scientific) software, and additional statistical analysis conducted by Prism v7.05 (GraphPad). Acetyl-CoA values were normalized to cell number and reported as pmol/10^5 cells.

Steady-state targeted metabolomics analysis of SIRT5 depletion

Melanoma cell lines infected with a control (pLKO.1 empty vector), SIRT5 KD1 or KD2 virus were cultured for 72 hrs. in complete growth medium on 10cm dishes in biological sextuplicate. Three dishes were reserved for metabolite collection, and three dishes were harvested in protein sample buffer (62.5mM Tris pH 6.8, 2% SDS, 10% glycerol) for protein quantification. A complete medium change was performed two hrs. prior to metabolite collection. Cells were washed twice in 2ml of PBS; one wash at room temperature and one at 4ºC. Taking care to aspirate all remaining liquid, plates were placed onto dry ice to cool before incubating in 4ml of 80% methanol for 10 mins. Plates were then scrape-harvested, and lysates transferred to 15 ml conical tubes. Lysates were centrifuged at 200 x g for 10 mins. For all experiments, the quantity of the metabolite fraction analyzed was adjusted to the corresponding average protein concentration. Liquid chromatography coupled-tandem mass spectrometry (LC-MS/MS) was employed for the detection of relative metabolite levels (86). Samples were analyzed on a 6490 Triple Quadrupole (QqQ) LC-MS against a targeted panel of 225 metabolites run in positive and negative modes. Agilent MassHunter Optimizer and Workstation Software LC-MS Data Acquisition for 6400 Series Triple Quadrupole B.08.00 was used for standard optimization and data acquisition. Agilent MassHunter Workstation Software Quantitative Analysis Version B.0700 for QqQ was used for initial raw data extraction and analysis. Each MRM transition and its retention time of left delta and right delta was 1 min. Additional parameters include mass extraction window of 0.05 Da right and left from the extract m/z, Agile2 integrator algorithm, peak filter of 100 counts, noise algorithm RMS, noise SD multiplier of 5 min, S/N 3, Accuracy Max 20% max %Dev, and Quadratic/Cubic Savitzky-Golay smoothing algorithm with smoothing function width of 14 and Gaussian width of 5. Peak area values under 10,000 were discarded as noise. Remaining raw values for each metabolite were median-centered across all conditions for each cell line. The average and standard deviation were taken for all replicates, and Student's t-tests were conducted comparing each KD to the control. Data for each metabolite was

represented as log(2) fold change with relative standard deviation. Pathway enrichment studies of both up- and down-regulated signaling were completed using Metaboanalyst and represented as log10(p-value) (87).

CM-H2DCFDA staining for ROS measurement

A2058 cells were plated at a density of $1x10^6$ per well of two six-well plates. Three wells were transduced each with either a lentivirus expressing a non-silencing shRNA (control) or one of two shRNAs targeting *SIRT5* (KD1 or KD2). Ninety-six hrs. after transduction, CM-H2DCFDA (ThermoFisher) was added to a final concentration of 5μM and incubated for 30 minutes in a humidified chamber at 37ºC. Cells were analyzed by flow cytometry using a BD FACSCalibur and results were plotted using FlowJo 10.2 analysis software.

Co-immunoprecipitation of SIRT5 with MTHFD1L

A2058 whole-cell protein extracts were prepared in protein lysis buffer (50mM Tris pH 7.4, 150mM NaCl, 1% Triton X-100, 0.5% NP40, 10% Glycerol) supplemented with 1μM TSA, 10mM nicotinamide, PhosStop cocktail (Roche), and protease inhibitor cocktail (Roche). Lysates were sonicated for 30 seconds using a Branson Sonifier set to output “2.” Lysates were then clarified by centrifugation at 15,000rcf for 30 minutes at 4ºC. Protein concentrations were determined using DC Protein Assay (Bio-Rad). Equivalent amounts (1mg) of total protein were mixed with the indicated amount (or 5μg) of biotinylated anti-SIRT5 antibody or normal rabbit IgG, and 20μl of protein A magnetic beads (Pierce), equilibrated in lysis buffer. After overnight rotation at 4ºC, samples were washed 4 times in 1ml of lysis buffer. Following the final wash, samples were boiled in 62.5mM Tris pH 6.8, 2% SDS, and 10% glycerol, supplemented with 710mM β-mercaptoethanol and 0.01% (w/v) bromophenol blue for 5 mins, and fractionated by

SDS-PAGE, followed by electrophoretic transfer and immunoblotting with the indicated antibodies.

Measurement of Oxygen consumption, Extracellular acidification, and Real-Time ATP production rate

Oxygen consumption rate (OCR), Extracellular acidification rate (ECAR), and Real-Time ATP production rate were measured using the XFe96 Extracellular Flux Analyzer (Seahorse Bioscience, Agilent Technologies, Santa Clara, CA). To measure glucose-dependent mitochondrial respiration, mitochondrial stress tests were performed to measure OCR per manufacturer's instructions. Briefly, 72 hrs. post-transduction, $4x10^4$ A375 or A2058 cells were plated in DMEM complete media supplemented with 10% heat-inactivated FBS into each well of a 96-well Seahorse microplate. Cells were then incubated in 5% CO_2 at 37ºC for 24 hrs. Following incubation, cells were washed twice, incubated in non-CO_2 incubator at 37ºC, and analyzed in XF assay media (non-buffered DMEM containing 25mM glucose, 2mM L-glutamine, and 1mM sodium pyruvate, pH 7.4) at 37ºC, under basal conditions and in response to 2µM oligomycin (Sigma), 1µM fluoro-carbonyl cyanide phenylhydrazone (FCCP) (Sigma) and 0.5µM rotenone (Sigma)/0.5µM antimycin A (Sigma). Data were analyzed by the Seahorse XF Cell Mito Stress Test Report Generator. OCR (pmol O_2/min) values were normalized to the protein content.

To measure glutamine-dependent mitochondrial respiration, mitochondrial stress test was performed to measure OCR as per manufacturer's instructions. Briefly, 72 hrs. post-transduction, $4x10^4$ A375, A2058 or SK-MEL-2 cells were plated in DMEM complete media supplemented with 10% heat-inactivated FBS into each well of a 96-well Seahorse microplate. Cells were then incubated in 5% CO_2 at 37ºC for 24 hrs. Following incubation, cells were washed twice, incubated (in non-CO_2 incubator at 37ºC), and analyzed in XF assay media (non-

buffered DMEM containing 4 mM L-glutamine, and 1 mM sodium pyruvate, pH 7.4) at 37ºC, under basal conditions and in response to 2μM oligomycin (Sigma), 1μM fluoro-carbonyl cyanide phenylhydrazone (FCCP) (Sigma) and 0.5μM rotenone (Sigma)/0.5μM antimycin A (Sigma). Data were analyzed by the Seahorse XF Cell Mito Stress Test Report Generator. OCR (pmol O_2/min) values were normalized to protein content.

ECAR values were measured by performing glycolysis stress tests according to manufacturer's instructions. Briefly, 72 hrs. post-transduction, $4x10^4$ A375 and A2058 cells were plated in DMEM complete media supplemented with 10% heat-inactivated FBS into each well of a 96-well Seahorse microplate. Cells were then incubated in 5% CO_2 at 37ºC for 24 hrs. Following incubation, cells were washed twice, incubated in a non-CO_2 incubator at 37ºC, and analyzed in XF assay media (non-buffered DMEM containing 2mM L-glutamine, pH 7.4) at 37ºC, under basal conditions and in response to 10mM glucose (Sigma), 2μM oligomycin (Sigma), and 50mM 2-deoxy-D-glucose (Sigma). Data were analyzed by the Seahorse XF Cell Glycolysis Stress Test Report Generator. ECAR (mpH/min) values were normalized to protein content.

The Seahorse XF Real-Time ATP Rate Assay Kit (Agilent) was used to simultaneously measure the basal ATP production rates from mitochondrial respiration and glycolysis. The assay was performed per manufacturer's instructions. Briefly, 72 hrs. post-transduction, $4x10^4$ A375 and A2058 cells were plated in DMEM complete media supplemented with 10% heat-inactivated FBS into each well of a 96-well Seahorse microplate. Cells were then incubated in 5% CO_2 at 37ºC for 24 hrs. Following incubation, cells were washed twice, incubated in a non-CO_2 incubator at 37ºC, and analyzed in XF assay media (non-buffered DMEM containing 10mM glucose, 2mM L-glutamine, and 1mM sodium pyruvate, pH 7.4) at 37ºC, under basal conditions and in response to 1.5μM oligomycin, and 0.5μM rotenone/0.5μM antimycin A. Data were

analyzed by the Seahorse XF Real-Time ATP Rate Assay Report Generator. ATP production rates were normalized to protein content.

JC-1 Mitochondrial membrane potential assay

At 96 hrs. post-transduction approximately $2x10^5$ A2058 cells in 100µl warm PBS were transferred into tube and stained with 10 µg/ml of JC-1 dye (AnaSpec). An additional 100µl from control cells were treated with 200 µM FCCP, a mitochondrial uncoupler, which depolarizes mitochondrial membrane potential, and used as a positive control. After 30 minutes of staining, cells were centrifuged to remove excess JC-1, washed twice with warm PBS and resuspended in 100µl of warm PBS. Cells were transferred into black 96-well plates and absorbance measured at 535nm (excitation)/595nm (emission) (aggregate, red) and 485nm (excitation)/435nm (emission) (monomer, green) using a H1 Synergy plate reader. The data are presented as a ratio of red to green fluorescence.

[$^{13}C_6$] Glucose, [$^{13}C_5$] Glutamine and [$^{15}N_2$] Glutamine Labelling for Metabolic Flux

Glucose and glutamine labelling were carried out as described previously (48). Briefly, 72 hrs. after transduction with pLKO control, pLKO *SIRT5* KD1, or pLKO *SIRT5* KD2, cells were trypsinized and plated in triplicate in 6-well dishes at a density of $1x10^6$ cells per well. Culture medium was replaced with [$^{13}C_6$] glucose, [$^{13}C_5$] glutamine or [$^{15}N_2$] glutamine labelling medium for 6 hours. Glucose labeling medium consisted of: MEM (1 g/L glucose; Gibco) supplemented with 1 g/L [U-$^{13}C_6$] glucose (Sigma), 10% v/v fetal bovine serum, 2 mM L-glutamine, 1% v/v pen/strep solution, and 1% MEM non-essential amino acids. Glutamine labeling medium was prepared as the glucose labeling medium, except an additional 1 g/L of unlabeled glucose, 1 mM unlabeled L-glutamine, and 1 mM [U-$^{13}C_5$] L-glutamine (Sigma) or 1 mM [$^{15}N_2$] L-glutamine (Sigma) was added. After 6 hours, cells were washed with cold PBS, then 0.45 ml of 50% methanol:50% water containing the internal standard, 20 µM L-norvaline (Sigma) was added to

each well. Plates were frozen on dry ice for 30 minutes and thawed on ice for 10 minutes. The cell suspension was transferred to a microfuge tube followed by the addition of 0.225 ml chloroform. Samples were vortexed, then centrifuged at 20,000rcf for 5 minutes at 4°C. The top layer was transferred to a fresh tube and dried in a Speedvac. Samples were then shipped to the Sanford Burnham Prebys Medical Discovery Institute (La Jolla, CA) for GC/MS-based metabolic profiling. Derivatization of metabolites, GC/MS settings, and data analysis for stable isotope labeling and metabolite quantification were as described (51). Metabolite quantities were determined using mass ion peak areas corresponding to unlabeled metabolites, and then corrected for the fraction of a metabolite that was ^{13}C or ^{15}N labeled to yield the total (labeled plus unlabeled) cellular quantity for that metabolite. This amount was normalized to total cellular protein.

Statistical Analysis

All statistical analyses were performed using Prism graphing software (Graphpad). Unless otherwise noted, $p \leq 0.05$ produced from an unpaired Student's t-test was considered significant.

Study approval

All mice were housed at the Biomedical Science Research Building (UM). All vertebrate animal experiments were approved by and performed in accordance with the regulations of the University Committee on Use and Care of Animals.

Author Contributions:

WG, LR, AM, MES, AG, SK, MA, ASAM, CHC, NK, KAM, HJL, LZ, PS, ST, ELV, SI, MW, JSW, HPS, RAS, ALP, AA, RAS, MSS, DAS, DRF, MWB, SC, ZNC, MV, NWS, MHR, ALO, CAL performed experiments and/or analyzed data. WG and DBL interpreted data, wrote and revised the paper. WG made the figures. DBL supervised overall design and study interpretation.

Acknowledgements: Funding: Melanoma Research Alliance (DL and CAL), NIH R01GM101171, AACR-Bayer (17-80-44-LOMB), DoD CA17068 and NF17004 (DL), and Rogel Cancer Center. Use of the Rogel Cancer Center shared resources is also gratefully acknowledged by DL and CAL (P30 CA46592). SK was supported in part through an award from the Pablove Foundation. CAL was supported by a 2017 AACR NextGen Grant for Transformative Cancer Research (17-20-01-LYSS) and an ACS Research Scholar Grant (RSG-18-186-01). Metabolomics studies performed at the University of Michigan were supported by NIH grant DK097153. ALP is supported by the Highlands and Islands Enterprise (HMS9353763); MSS holds a fellowship (APP1106491) from the National Health and Medical Research Council (NHMRC). WG, AG, and LR were supported by NIH T32 awards (WG: AG000114, HL007853 and AR007917; AG: AG000114 and GM113900; LR NL007517). NWS was supported by R01GM132261. ST was funded by American Diabetes Association postdoctoral fellowship #1-18-PDF-144. RAS and JSW are supported by the Australian National Health and Medical Research Council Fellowship program. Support from colleagues at Melanoma Institute Australia and the Royal Prince Alfred Hospital is also gratefully acknowledged. HPS holds an NHMRC MRFF Next Generation Clinical Researchers Program Practitioner Fellowship (APP1137127). The SBP Cancer Metabolism Core is supported by National Cancer Institute Cancer Center Support Grant P30 030199. Dr. Jeongsoon Park is acknowledged for technical contributions early in the project. Dr. Scott Pletcher (UM) is acknowledged for assistance with statistical analysis. Dr. Emily Bernstein (Icahn School of Medicine at Mount Sinai) is acknowledged for generously providing cell lines. Drs. David Fisher (MGH Cancer Center/Harvard Medical School) and Kathryn Wellen (University of Pennsylvania) are gratefully acknowledged for helpful discussions. Olga Zagnitko is acknowledged for assistance with GC/MS measurements. GEO submission of RNA-seq data is in process.

References

1. Siegel RL, Miller KD, and Jemal A. Cancer statistics, 2019. *CA: A Cancer Journal for Clinicians.* 2019;69(1):7-34.
2. Dharmadhikari N, Mehnert JM, and Kaufman HL. Oncolytic virus immunotherapy for melanoma. *Curr Treat Options Oncol.* 2015;16(3):326.
3. Guy GP, and Ekwueme DU. Years of potential life lost and indirect costs of melanoma and non-melanoma skin cancer: a systematic review of the literature. *Pharmacoeconomics.* 2011;29(10):863-74.
4. Larkin J, Chiarion-Sileni V, Gonzalez R, Grob JJ, Rutkowski P, Lao CD, et al. Five-Year Survival with Combined Nivolumab and Ipilimumab in Advanced Melanoma. *N Engl J Med.* 2019;381(16):1535-46.
5. Singh M, Durairaj P, and Yeung J. Uveal Melanoma: A Review of the Literature. *Oncology and Therapy.* 2018;6(1):87-104.
6. Bringman-Rodenbarger LR, Guo AH, Lyssiotis CA, and Lombard DB. Emerging Roles for SIRT5 in Metabolism and Cancer. *Antioxid Redox Signal.* 2018;28(8):677-90.
7. Du J, Zhou Y, Su X, Yu JJ, Khan S, Jiang H, et al. Sirt5 is a NAD-dependent protein lysine demalonylase and desuccinylase. *Science.* 2011;334(6057):806-9.
8. Rardin MJ, He W, Nishida Y, Newman JC, Carrico C, Danielson SR, et al. SIRT5 regulates the mitochondrial lysine succinylome and metabolic networks. *Cell Metab.* 2013;18(6):920-33.
9. North BJ, Marshall BL, Borra MT, Denu JM, and Verdin E. The human Sir2 ortholog, SIRT2, is an NAD+-dependent tubulin deacetylase. *Mol Cell.* 2003;11(2):437-44.
10. Park J, Chen Y, Tishkoff DX, Peng C, Tan M, Dai L, et al. SIRT5-mediated lysine desuccinylation impacts diverse metabolic pathways. *Mol Cell.* 2013;50(6):919-30.

11. Tan M, Peng C, Anderson Kristin A, Chhoy P, Xie Z, Dai L, et al. Lysine Glutarylation Is a Protein Posttranslational Modification Regulated by SIRT5. *Cell Metabolism.* 2014;19(4):605-17.

12. Peng C, Lu Z, Xie Z, Cheng Z, Chen Y, Tan M, et al. The first identification of lysine malonylation substrates and its regulatory enzyme. *Mol Cell Proteomics.* 2011;10(12):M111 012658 1-12.

13. Nishida Y, Rardin MJ, Carrico C, He W, Sahu AK, Gut P, et al. SIRT5 Regulates both Cytosolic and Mitochondrial Protein Malonylation with Glycolysis as a Major Target. *Mol Cell.* 2015;59(2):321-32.

14. Lombard DB, Alt FW, Cheng HL, Bunkenborg J, Streeper RS, Mostoslavsky R, et al. Mammalian Sir2 homolog SIRT3 regulates global mitochondrial lysine acetylation. *Mol Cell Biol.* 2007;27(24):8807-14.

15. Yu J, Sadhukhan S, Noriega LG, Moullan N, He B, Weiss RS, et al. Metabolic characterization of a Sirt5 deficient mouse model. *Sci Rep.* 2013;3:2806.

16. Kumar S, and Lombard DB. Functions of the sirtuin deacylase SIRT5 in normal physiology and pathobiology. *Critical reviews in biochemistry and molecular biology.* 2018;53(3):311-34.

17. Boylston JA, Sun J, Chen Y, Gucek M, Sack MN, and Murphy E. Characterization of the cardiac succinylome and its role in ischemia-reperfusion injury. *J Mol Cell Cardiol.* 2015;88:73-81.

18. Sadhukhan S, Liu X, Ryu D, Nelson OD, Stupinski JA, Li Z, et al. Metabolomics-assisted proteomics identifies succinylation and SIRT5 as important regulators of cardiac function. *Proc Natl Acad Sci U S A.* 2016;113(16):4320-5.

19. Hershberger KA, Abraham DM, Martin AS, Mao L, Liu J, Gu H, et al. Sirtuin 5 is required for mouse survival in response to cardiac pressure overload. *J Biol Chem.* 2017;292(48):19767-81.

20. Hershberger KA, Abraham DM, Liu J, Locasale JW, Grimsrud PA, and Hirschey MD. Ablation of Sirtuin5 in the postnatal mouse heart results in protein succinylation and normal survival in response to chronic pressure overload. *J Biol Chem.* 2018;293(27):10630-45.

21. Roth M, and Chen WY. Sorting out functions of sirtuins in cancer. *Oncogene.* 2014;33(13):1609-20.

22. Lu W, Zuo Y, Feng Y, and Zhang M. SIRT5 facilitates cancer cell growth and drug resistance in non-small cell lung cancer. *Tumour biology : the journal of the International Society for Oncodevelopmental Biology and Medicine.* 2014.

23. Lv XB, Liu L, Cheng C, Yu B, Xiong L, Hu K, et al. SUN2 exerts tumor suppressor functions by suppressing the Warburg effect in lung cancer. *Sci Rep.* 2015;5:17940.

24. Lin ZF, Xu HB, Wang JY, Lin Q, Ruan Z, Liu FB, et al. SIRT5 desuccinylates and activates SOD1 to eliminate ROS. *Biochem Biophys Res Commun.* 2013;441(1):191-5.

25. Zhou L, Wang F, Sun R, Chen X, Zhang M, Xu Q, et al. SIRT5 promotes IDH2 desuccinylation and G6PD deglutarylation to enhance cellular antioxidant defense. *EMBO Rep.* 2016;17(6):811-22.

26. Yang X, Wang Z, Li X, Liu B, Liu M, Liu L, et al. SHMT2 Desuccinylation by SIRT5 Drives Cancer Cell Proliferation. *Cancer Res.* 2018;78(2):372-86.

27. Chang L, Xi L, Liu Y, Liu R, Wu Z, and Jian Z. SIRT5 promotes cell proliferation and invasion in hepatocellular carcinoma by targeting E2F1. *Molecular medicine reports.* 2017.

28. Zhang R, Wang C, Tian Y, Yao Y, Mao J, Wang H, et al. SIRT5 Promotes Hepatocellular Carcinoma Progression by Regulating Mitochondrial Apoptosis. *J Cancer.* 2019;10(16):3871-82.

29. Greene KS, Lukey MJ, Wang X, Blank B, Druso JE, Lin MJ, et al. SIRT5 stabilizes mitochondrial glutaminase and supports breast cancer tumorigenesis. *Proc Natl Acad Sci U S A.* 2019.

30. Pavlova NN, and Thompson CB. The Emerging Hallmarks of Cancer Metabolism. *Cell Metab.* 2016;23(1):27-47.

31. Li F, He X, Ye D, Lin Y, Yu H, Yao C, et al. NADP(+)-IDH Mutations Promote Hypersuccinylation that Impairs Mitochondria Respiration and Induces Apoptosis Resistance. *Mol Cell.* 2015;60(4):661-75.

32. Xu YS, Liang JJ, Wang Y, Zhao XJ, Xu L, Xu YY, et al. STAT3 Undergoes Acetylation-dependent Mitochondrial Translocation to Regulate Pyruvate Metabolism. *Sci Rep.* 2016;6:39517.

33. Hartman ML, and Czyz M. Pro-Survival Role of MITF in Melanoma. *Journal of Investigative Dermatology.* 2015;135(2):352-8.

34. Zhuang D, Mannava S, Grachtchouk V, Tang WH, Patil S, Wawrzyniak JA, et al. C-MYC overexpression is required for continuous suppression of oncogene-induced senescence in melanoma cells. *Oncogene.* 2008;27(52):6623-34.

35. North JP, Vetto JT, Murali R, White KP, White CR, Jr., and Bastian BC. Assessment of copy number status of chromosomes 6 and 11 by FISH provides independent prognostic information in primary melanoma. *The American journal of surgical pathology.* 2011;35(8):1146-50.

36. Santos GC, Zielenska M, Prasad M, and Squire JA. Chromosome 6p amplification and cancer progression. *J Clin Pathol.* 2007;60(1):1-7.

37. Cancer Genome Atlas N. Genomic Classification of Cutaneous Melanoma. *Cell.* 2015;161(7):1681-96.

38. Hodis E, Watson IR, Kryukov GV, Arold ST, Imielinski M, Theurillat JP, et al. A landscape of driver mutations in melanoma. *Cell.* 2012;150(2):251-63.

39. Stark M, and Hayward N. Genome-wide loss of heterozygosity and copy number analysis in melanoma using high-density single-nucleotide polymorphism arrays. *Cancer Res.* 2007;67(6):2632-42.

40. Dutton-Regester K, Aoude LG, Nancarrow DJ, Stark MS, O'Connor L, Lanagan C, et al. Identification of TFG (TRK-fused gene) as a putative metastatic melanoma tumor suppressor gene. *Genes, chromosomes & cancer.* 2012;51(5):452-61.

41. Stark MS, Tan JM, Tom L, Jagirdar K, Lambie D, Schaider H, et al. Whole-Exome Sequencing of Acquired Nevi Identifies Mechanisms for Development and Maintenance of Benign Neoplasms. *The Journal of investigative dermatology.* 2018;138(7):1636-44.

42. Shain AH, Yeh I, Kovalyshyn I, Sriharan A, Talevich E, Gagnon A, et al. The Genetic Evolution of Melanoma from Precursor Lesions. *New England Journal of Medicine.* 2015;373(20):1926-36.

43. Luebker SA, and Koepsell SA. Diverse Mechanisms of BRAF Inhibitor Resistance in Melanoma Identified in Clinical and Preclinical Studies. *Frontiers in oncology.* 2019;9:268.

44. Meeth K, Wang JX, Micevic G, Damsky W, and Bosenberg MW. The YUMM lines: a series of congenic mouse melanoma cell lines with defined genetic alterations. *Pigment Cell & Melanoma Research.* 2016;29(5):590-7.

45. Dankort D, Curley DP, Cartlidge RA, Nelson B, Karnezis AN, Damsky WE, Jr., et al. Braf(V600E) cooperates with Pten loss to induce metastatic melanoma. *Nat Genet.* 2009;41(5):544-52.

46. Buler M, Aatsinki SM, Izzi V, Uusimaa J, and Hakkola J. SIRT5 is under the control of PGC-1alpha and AMPK and is involved in regulation of mitochondrial energy metabolism. *Faseb j.* 2014;28(7):3225-37.

47. Zhang Y, Bharathi SS, Rardin MJ, Lu J, Maringer KV, Sims-Lucas S, et al. Lysine desuccinylase SIRT5 binds to cardiolipin and regulates the electron transport chain. *J Biol Chem.* 2017;292(24):10239-49.

48. Scott DA, Richardson AD, Filipp FV, Knutzen CA, Chiang GG, Ronai ZA, et al. Comparative metabolic flux profiling of melanoma cell lines: beyond the Warburg effect. *J Biol Chem.* 2011;286(49):42626-34.

49. Filipp FV, Scott DA, Ronai ZA, Osterman AL, and Smith JW. Reverse TCA cycle flux through isocitrate dehydrogenases 1 and 2 is required for lipogenesis in hypoxic melanoma cells. *Pigment Cell Melanoma Res.* 2012;25(3):375-83.

50. Filipp FV, Ratnikov B, De Ingeniis J, Smith JW, Osterman AL, and Scott DA. Glutamine-fueled mitochondrial metabolism is decoupled from glycolysis in melanoma. *Pigment Cell Melanoma Res.* 2012;25(6):732-9.

51. Ratnikov B, Aza-Blanc P, Ronai ZA, Smith JW, Osterman AL, and Scott DA. Glutamate and asparagine cataplerosis underlie glutamine addiction in melanoma. *Oncotarget.* 2015;6(10):7379-89.

52. Qin JZ, Xin H, and Nickoloff BJ. Targeting glutamine metabolism sensitizes melanoma cells to TRAIL-induced death. *Biochem Biophys Res Commun.* 2010;398(1):146-52.

53. Qin JZ, Xin H, and Nickoloff BJ. 2-deoxyglucose sensitizes melanoma cells to TRAIL-induced apoptosis which is reduced by mannose. *Biochem Biophys Res Commun.* 2010;401(2):293-9.

54. Garraway LA, Widlund HR, Rubin MA, Getz G, Berger AJ, Ramaswamy S, et al. Integrative genomic analyses identify MITF as a lineage survival oncogene amplified in malignant melanoma. *Nature.* 2005;436(7047):117-22.

55. Seoane M, Buhs S, Iglesias P, Strauss J, Puller AC, Muller J, et al. Lineage-specific control of TFIIH by MITF determines transcriptional homeostasis and DNA repair. *Oncogene.* 2019;38(19):3616-35.

56. Duarte NC, Becker SA, Jamshidi N, Thiele I, Mo ML, Vo TD, et al. Global reconstruction of the human metabolic network based on genomic and bibliomic data. *Proc Natl Acad Sci U S A.* 2007;104(6):1777-82.

57. Chandrasekaran S, Zhang J, Sun Z, Zhang L, Ross CA, Huang YC, et al. Comprehensive Mapping of Pluripotent Stem Cell Metabolism Using Dynamic Genome-Scale Network Modeling. *Cell Rep.* 2017;21(10):2965-77.

58. Shlomi T, Cabili MN, Herrgard MJ, Palsson BO, and Ruppin E. Network-based prediction of human tissue-specific metabolism. *Nature biotechnology.* 2008;26(9):1003-10.

59. Wellen KE, Hatzivassiliou G, Sachdeva UM, Bui TV, Cross JR, and Thompson CB. ATP-citrate lyase links cellular metabolism to histone acetylation. *Science.* 2009;324(5930):1076-80.

60. Sivanand S, Viney I, and Wellen KE. Spatiotemporal Control of Acetyl-CoA Metabolism in Chromatin Regulation. *Trends Biochem Sci.* 2018;43(1):61-74.

61. Snyder NW, Tombline G, Worth AJ, Parry RC, Silvers JA, Gillespie KP, et al. Production of stable isotope-labeled acyl-coenzyme A thioesters by yeast stable isotope labeling by essential nutrients in cell culture. *Analytical biochemistry.* 2015;474:59-65.

62. Frey AJ, Feldman DR, Trefely S, Worth AJ, Basu SS, and Snyder NW. LC-quadrupole/Orbitrap high-resolution mass spectrometry enables stable isotope-resolved simultaneous quantification and (1)(3)C-isotopic labeling of acyl-coenzyme A thioesters. *Anal Bioanal Chem.* 2016;408(13):3651-8.

63. Yang M, and Vousden KH. Serine and one-carbon metabolism in cancer. *Nat Rev Cancer.* 2016;16(10):650-62.

64. Gao X, Reid MA, Kong M, and Locasale JW. Metabolic interactions with cancer epigenetics. *Molecular Aspects of Medicine.* 2017;54:50-7.

65. Mailloux RJ, McBride SL, and Harper ME. Unearthing the secrets of mitochondrial ROS and glutathione in bioenergetics. *Trends Biochem Sci.* 2013;38(12):592-602.

66. Colak G, Pougovkina O, Dai L, Tan M, Te Brinke H, Huang H, et al. Proteomic and Biochemical Studies of Lysine Malonylation Suggest Its Malonic Aciduria-associated Regulatory Role in Mitochondrial Function and Fatty Acid Oxidation. *Mol Cell Proteomics.* 2015;14(11):3056-71.

67. Kumar S, and Lombard DB. Mitochondrial sirtuins and their relationships with metabolic disease and cancer. *Antioxid Redox Signal.* 2015;22(12):1060-77.

68. Hartman ML, and Czyz M. MITF in melanoma: mechanisms behind its expression and activity. *Cellular and Molecular Life Sciences.* 2015;72(7):1249-60.

69. Moon H, Zhu J, and White AC. Sirt5 is dispensable for Braf(V600E) -mediated cutaneous melanoma development and growth in vivo. *Exp Dermatol.* 2019;28(1):83-5.

70. Haq R, and Fisher DE. Biology and clinical relevance of the micropthalmia family of transcription factors in human cancer. *J Clin Oncol.* 2011;29(25):3474-82.

71. Wellbrock C, and Marais R. Elevated expression of MITF counteracts B-RAF-stimulated melanocyte and melanoma cell proliferation. *J Cell Biol.* 2005;170(5):703-8.

72. Becker JS, Nicetto D, and Zaret KS. H3K9me3-Dependent Heterochromatin: Barrier to Cell Fate Changes. *Trends in genetics : TIG.* 2016;32(1):29-41.

73. Schlicker C, Gertz M, Papatheodorou P, Kachholz B, Becker CFW, and Steegborn C. Substrates and Regulation Mechanisms for the Human Mitochondrial Sirtuins Sirt3 and Sirt5. *Journal of Molecular Biology.* 2008;382(3):790-801.

74. Sanson KR, Hanna RE, Hegde M, Donovan KF, Strand C, Sullender ME, et al. Optimized libraries for CRISPR-Cas9 genetic screens with multiple modalities. *Nat Commun.* 2018;9(1):5416.

75. Birsoy K, Wang T, Chen WW, Freinkman E, Abu-Remaileh M, and Sabatini DM. An Essential Role of the Mitochondrial Electron Transport Chain in Cell Proliferation Is to Enable Aspartate Synthesis. *Cell.* 2015;162(3):540-51.

76. Ran FA, Hsu PD, Wright J, Agarwala V, Scott DA, and Zhang F. Genome engineering using the CRISPR-Cas9 system. *Nat Protoc.* 2013;8(11):2281-308.

77. Sanjana NE, Shalem O, and Zhang F. Improved vectors and genome-wide libraries for CRISPR screening. *Nat Methods.* 2014;11(8):783-4.

78. Bousquet PF, Brana MF, Conlon D, Fitzgerald KM, Perron D, Cocchiaro C, et al. Preclinical evaluation of LU 79553: a novel bis-naphthalimide with potent antitumor activity. *Cancer Res.* 1995;55(5):1176-80.

79. Faustino-Rocha A, Oliveira PA, Pinho-Oliveira J, Teixeira-Guedes C, Soares-Maia R, da Costa RG, et al. Estimation of rat mammary tumor volume using caliper and ultrasonography measurements. *Lab Anim (NY).* 2013;42(6):217-24.

80. Dobin A, Davis CA, Schlesinger F, Drenkow J, Zaleski C, Jha S, et al. STAR: ultrafast universal RNA-seq aligner. *Bioinformatics.* 2013;29(1):15-21.

81. Liao Y, Smyth GK, and Shi W. featureCounts: an efficient general purpose program for assigning sequence reads to genomic features. *Bioinformatics.* 2014;30(7):923-30.

82. Quinlan AR, and Hall IM. BEDTools: a flexible suite of utilities for comparing genomic features. *Bioinformatics.* 2010;26(6):841-2.

83. Love MI, Huber W, and Anders S. Moderated estimation of fold change and dispersion for RNA-seq data with DESeq2. *Genome Biol.* 2014;15(12):550.

84. Shen F, Boccuto L, Pauly R, Srikanth S, and Chandrasekaran S. Genome-scale network model of metabolism and histone acetylation reveals metabolic dependencies of histone deacetylase inhibitors. *Genome Biol.* 2019;20(1):49.

85. Shen F, Cheek C, and Chandrasekaran S. Dynamic Network Modeling of Stem Cell Metabolism. *Methods Mol Biol.* 2019;1975:305-20.

86. Lee HJ, Kremer DM, Sajjakulnukit P, Zhang L, and Lyssiotis CA. A large-scale analysis of targeted metabolomics data from heterogeneous biological samples provides insights into metabolite dynamics. *Metabolomics.* 2019;15(7):103.

87. Chong J, Yamamoto M, and Xia J. MetaboAnalystR 2.0: From Raw Spectra to Biological Insights. *Metabolites.* 2019;9(3).

Figures

Figure 1

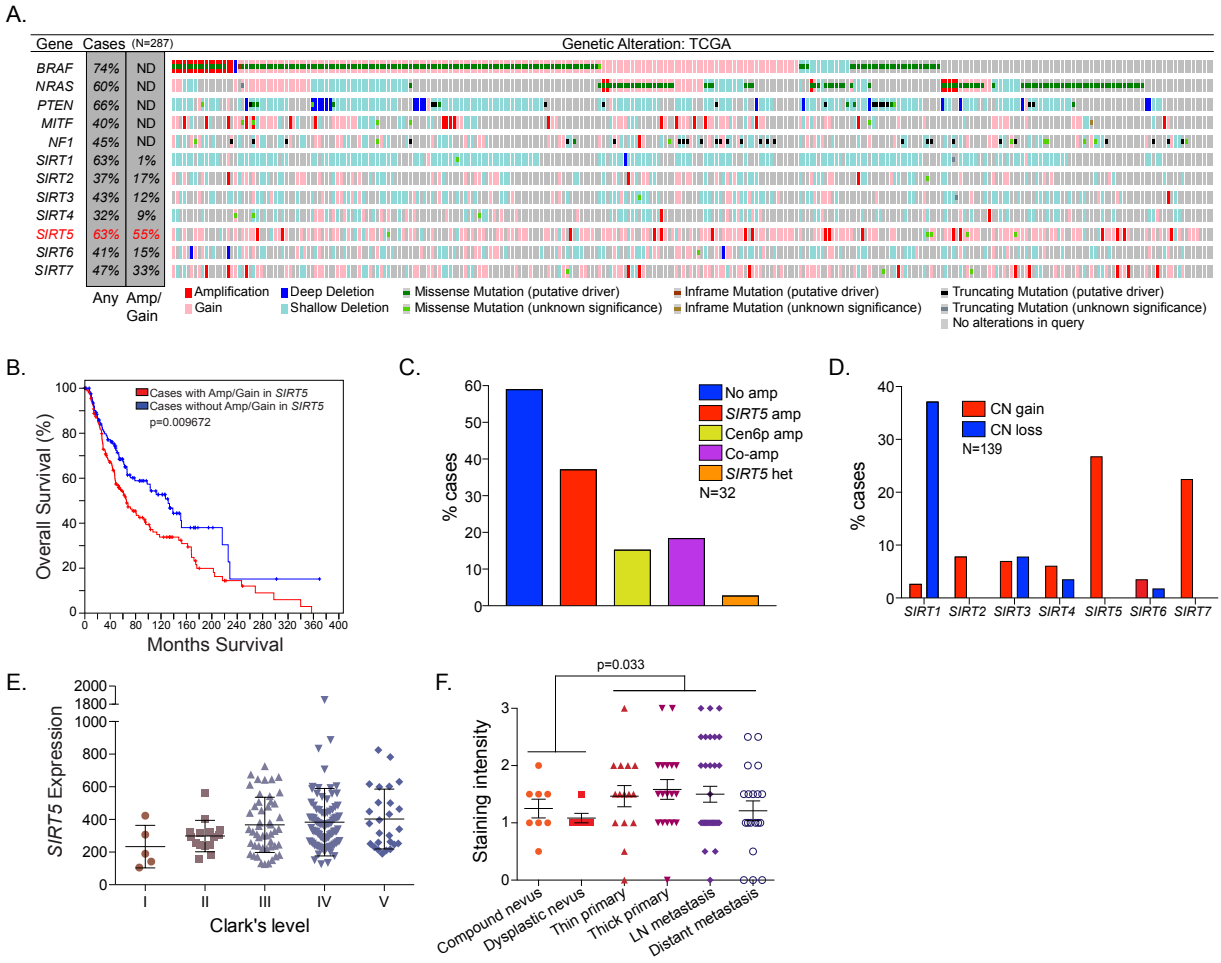

Figure 1 Increased *SIRT5* copy number in human melanoma.
A. Gain of extra *SIRT5* copies in melanoma. *BRAF, NRAS, PTEN, MITF, NF1* and other sirtuins are shown for comparison (n=287; data from TCGA, Provisional, analyzed on cBioPortal). ND, not determined. Percentage of samples with any genomic alteration (Any) or amplification or gain (Amp/Gain) is indicated. Graphed are any alterations queried for the indicated gene. Copy number gain indicates a low-level gain of a single additional copy, and amplification refers to high-level amplification (multiple extra copies). Results from the query (*GENE*: MUT AMP HOMDEL GAIN HETLOSS) in cBioPortal were analyzed and plotted. B. Kaplan–Meier analysis of overall survival in melanoma patients with or without copy number gain or amplification of *SIRT5*. Overall survival was analyzed using the query: *"SIRT5*: AMP GAIN." C. *SIRT5* (6p23) and centromere 6p (Cen6p) amplification (amp) or co-amplification (Co-amp) in melanoma, as assayed by FISH staining (n=32). D. Sirtuin gene copy number (CN) in human melanoma samples, as assayed by high density SNP array (n=139). E. *SIRT5* mRNA expression levels in melanoma correlate with Clark's level (p=0.0044, linear regression; p=0.037, ANOVA). F. SIRT5 protein levels are increased in melanoma relative to benign melanocytic lesions (p=0.0333, Chi-squared; n=14 nevi, n=87 melanoma). See also Figure S1 and Table S1.

Figure 2

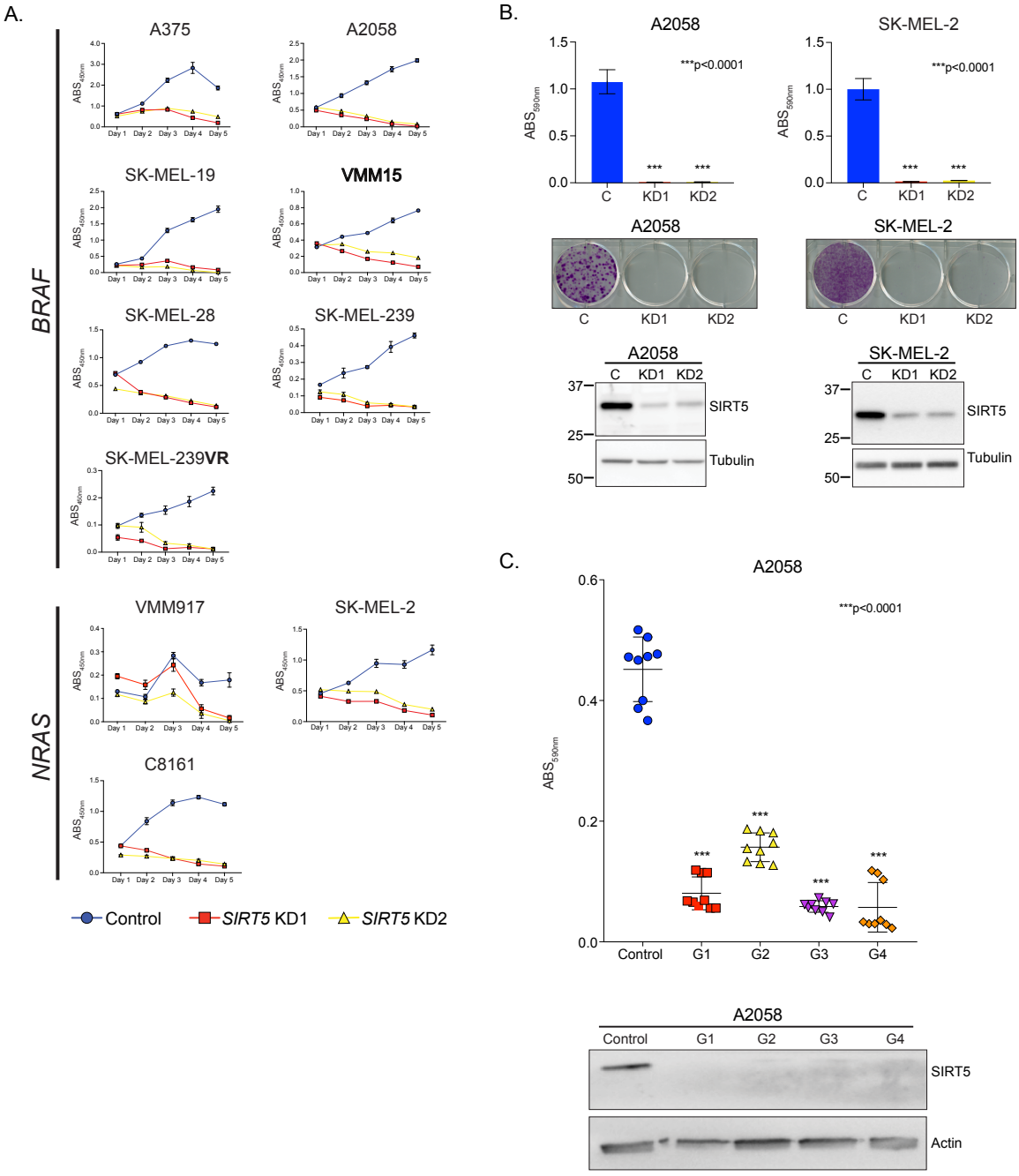

Figure 2 SIRT5 is required for melanoma cell growth and survival.
A. *BRAF* or *NRAS* mutant melanoma cell lines indicated were infected with a non-targeting shRNA (control) or one of two SIRT5 shRNAs (KD1 or KD2). Equivalent cell numbers were then plated 48 hrs. post-transduction into 96-well plates in the presence of puromycin. Cell mass was determined at the indicated timepoints via WST-1 assay, with absorbance measured at 450nm. Average results (n=6/timepoint) are graphed. Error bars represent standard deviation. Representative of 5/5 SIRT5 shRNAs tested (see also Figure 3B). B. SIRT5 KD results in significantly ($p<0.0001$) impaired colony formation by A2058 and SK-MEL-2 cells 12 days post-transduction. Cell mass was assayed using crystal violet staining, with absorbance measured at 590nm. Average of n=12 technical replicates results are plotted. Error bars represent SD. Representative crystal violet-stained wells are shown. Lower panel, representative immunoblot analysis demonstrating SIRT5 KD. C. Top panel, viability of A2058 cells transfected with the indicated CRISPR guide RNA (Control or G1-G4). Cell mass was assayed using crystal violet staining, with absorbance measured at 590nm. Average of n=9 technical replicates results are plotted. Error bars represent standard deviation. Bottom panel, representative immunoblot analysis confirming CRISPR-mediated SIRT5 loss (Control: empty vector).

Figure 3

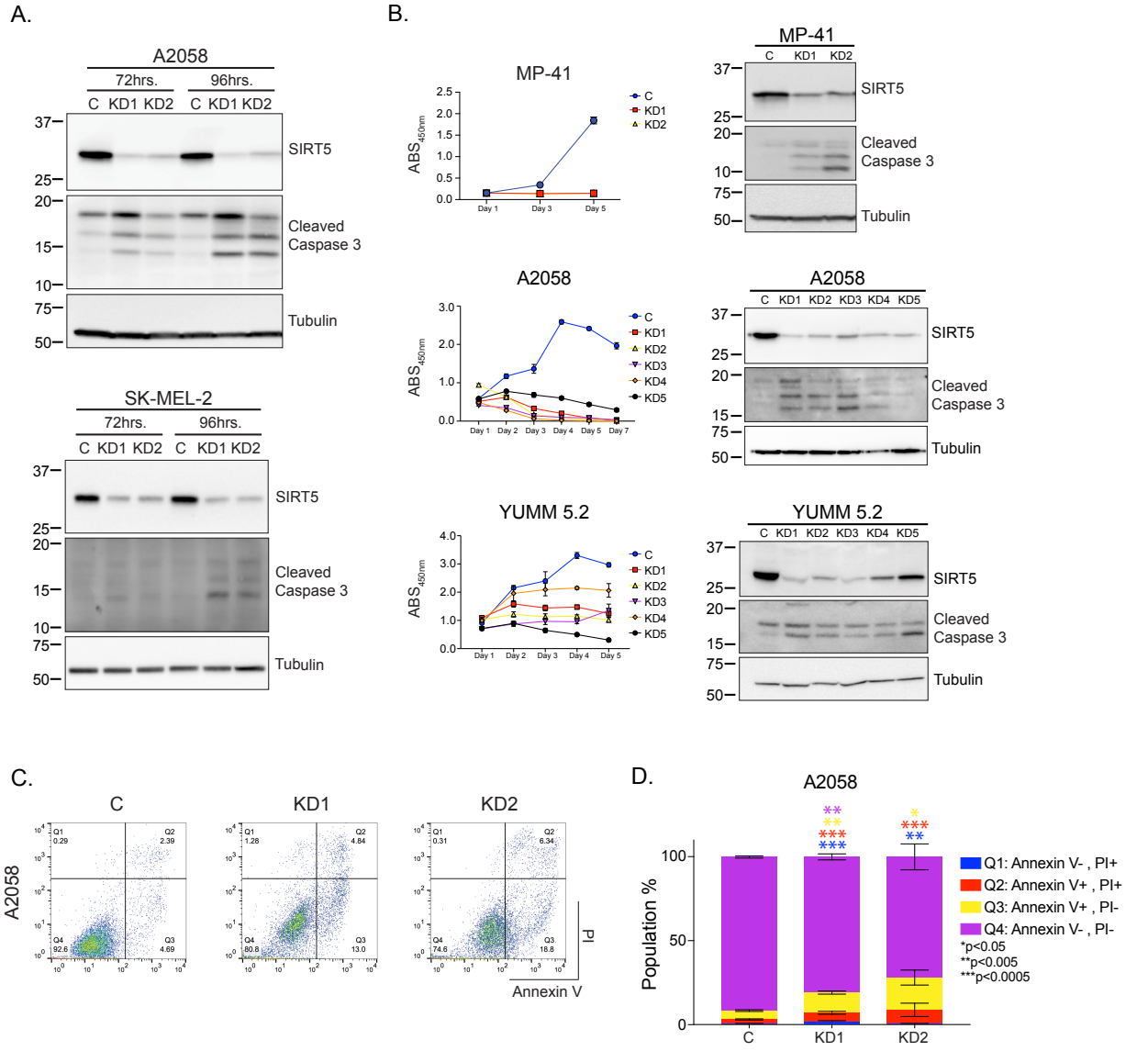

Figure 3 SIRT5 depletion rapidly induces apoptosis in melanoma cells.
A. Immunoblot analysis demonstrating induction of caspase 3 cleavage 72 and 96 hrs. post-transduction with shRNAs targeting SIRT5 (KD1 or KD2) in A2058 and SK-MEL-2 cell lines. B. Viability of MP-41, A2058 or YUMM5.2 cells infected with control (C) or one of five SIRT5 shRNAs (KD1-KD5) against human *SIRT5* (top and middle panels) or mouse *Sirt5* (bottom panel). Average results (n=6/time-point) are graphed. Error bars represent standard deviation. Right panels: immunoblot analysis demonstrating loss of SIRT5 and induction of caspase 3 cleavage following SIRT5 KD. C. Flow cytometric analysis of A2058 cells stained with Annexin V and propidium iodide (PI), as indicated, showing an increased fraction of Annexin V-positive cells 96 hrs. after SIRT5 KD. D. Average of n=3 technical replicates is graphed. Error bars represent (SD). Increased Annexin V$^+$ staining is observed in both the PI-positive and PI-negative populations.

Figure 4

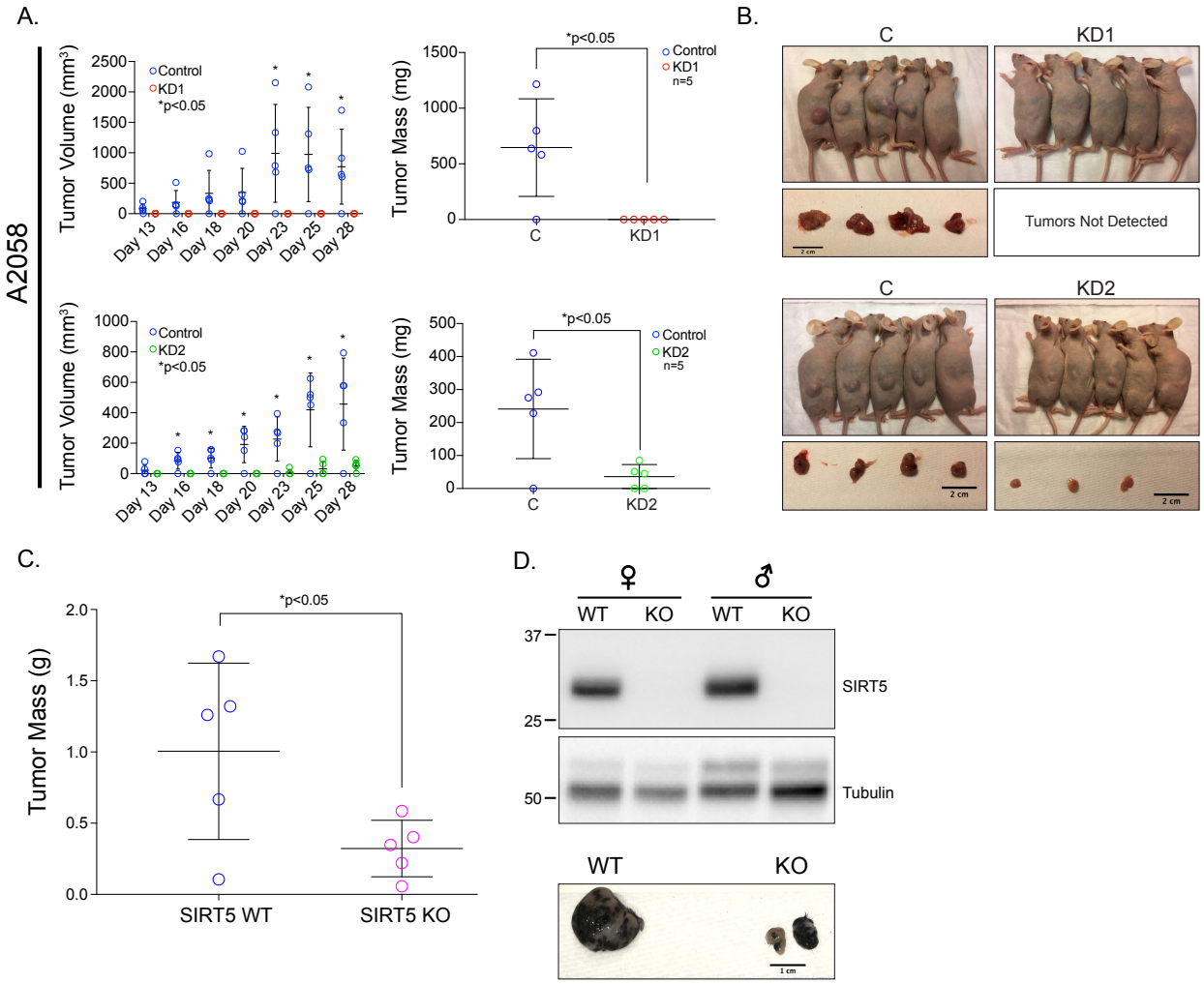

Figure 4 SIRT5 loss-of-function inhibits melanoma tumor growth *in vivo*.
A. SIRT5 depletion in A2058 cells results in attenuated xenograft tumor growth. Quantification of tumor size was initiated on day 13 after initial injection of cells (left panel). Tumor size was recorded with Vernier calipers on the days indicated. Each point represents the measurements on n=5 mice for each condition (C, KD1, or KD2). Pairwise representation of endpoint tumor size in each mouse within each group is plotted (right panel). Average tumor mass measurements at day 28 are plotted ($p<0.05$, paired two-tailed t-test for each group). Error bars represent SD. B. Mice were sacrificed, and tumors were dissected at 28 days after initial injection. Scale bar below tumors=2cm. C. SIRT5 deficiency attenuates tumor formation in an autochthonous melanoma model. *Sirt5* deficient-mice were bred into the *Braf*^{CA}*;Pten*$^{fl/fl}$*;Tyr::CreER* background (45). Melanomas were induced in littermate male *Sirt5* WT or *Sirt5* KO mice as shown by topical application of 4HT at ages 4-9 weeks; tumors were weighed following euthanasia. Averages of 5 sets of male mice are plotted ($p<0.05$, paired two-tailed t-test). Means ± SD are shown. D. SIRT5 immunoblot of a representative tumor from a SIRT5 WT or KO male or female mouse (left panel). Representative tumor from a SIRT5 WT or KO male mouse, as indicated, after 4HT induction (right panel). Scale bar=1cm.

Figure 5

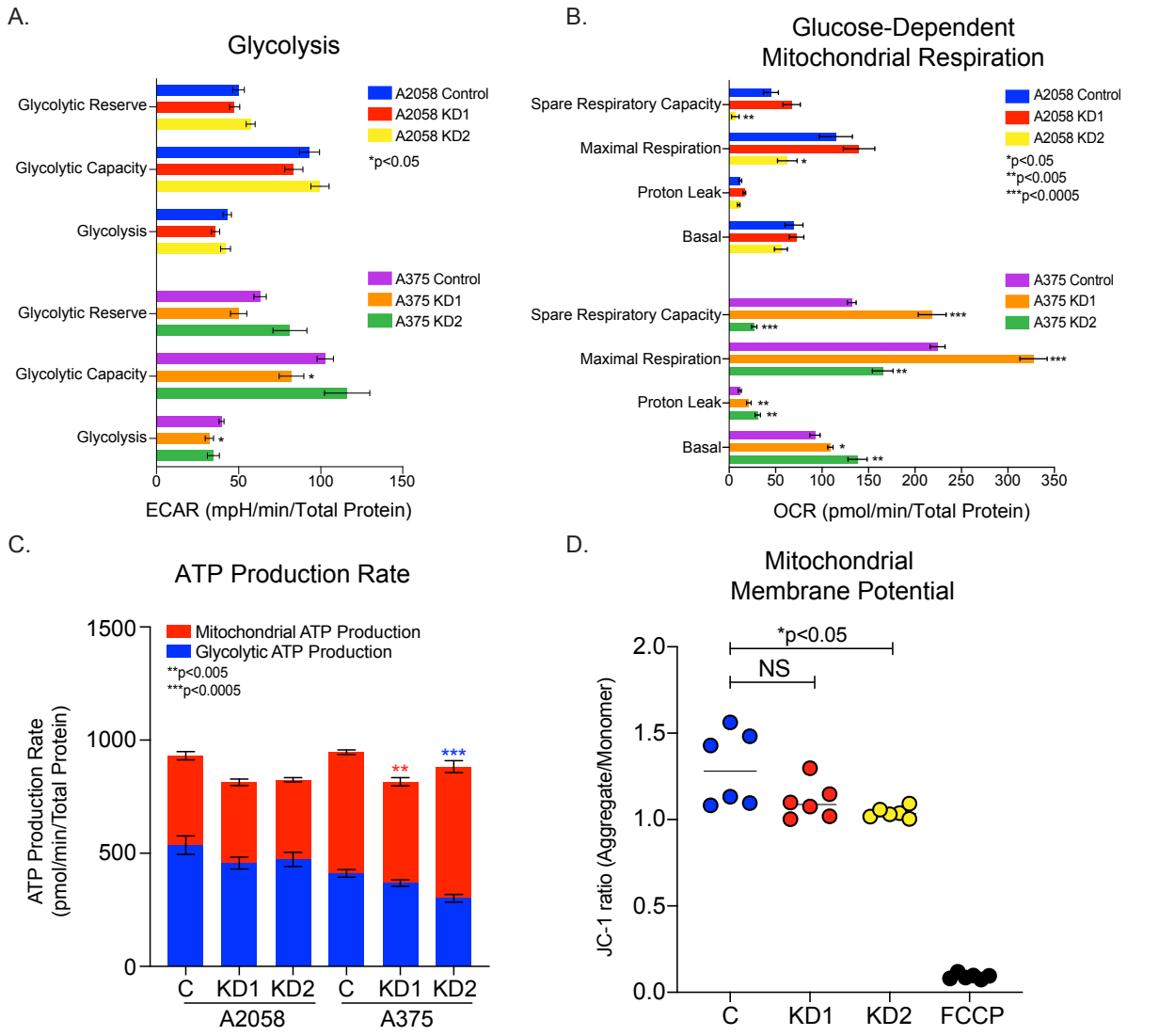

Figure 5 Bioenergetics are maintained upon SIRT5 loss in melanoma cells.
A2058 and A375 cells maintain glycolytic function (A.), glucose-dependent mitochondrial respiration (B.), and ATP production (C.) upon SIRT5 depletion compared to control cells. Mitochondrial respiration, glycolytic stress tests, and ATP production rates were measured at 96 hrs. post-transduction with shRNAs against SIRT5 using a Seahorse XFe96 Analyzer. All rates are normalized to total protein content per sample (N=5 for each assay). OCR, oxygen consumption rate; ECAR, extracellular acidification rate. Error bars represent SEM. D. Mitochondrial membrane potential is stable in A2058 cells after SIRT5 loss (C, control cells). Cells were incubated with JC-1, a dye which exhibits potential-dependent accumulation in mitochondria, indicated by a fluorescence emission shift from green to red. Mitochondrial depolarization is indicated by a decrease in the red:green (aggregate:monomer) fluorescence intensity ratio. FCCP, a mitochondrial uncoupler, depolarizes mitochondrial membrane potential and is used as a positive control.

Figure 6

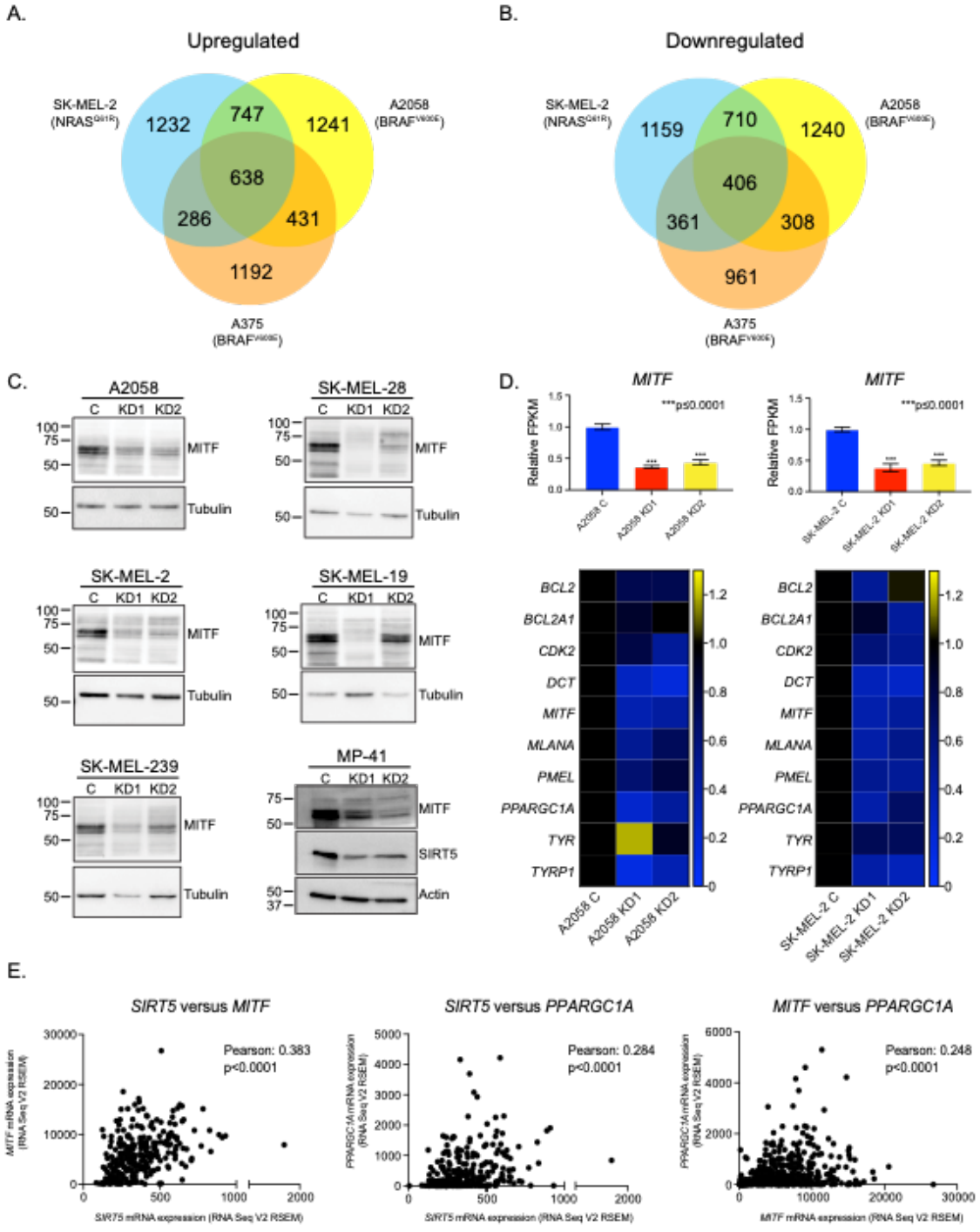

Figure 6 Expression of MITF and MITF target genes is dependent upon SIRT5.
Genes (A.) upregulated or (B.) downregulated upon SIRT5 KD. Only genes significantly ($p<0.05$) altered in both KDs in each cell line, as indicated, were scored. C. Immunoblot demonstrating loss of MITF expression 96 hrs. post-transduction with shRNAs targeting *SIRT5* (KD1 or KD2) compared to a non-targeting control (C) in 5 cutaneous and one uveal melanoma cell lines, as indicated. D. Relative FPKMs in A2058 and SK-MEL-2 cells demonstrate a loss of *MITF* (bar graphs, upper panels) and several *MITF* target gene transcripts upon SIRT5 KD (heatmaps, lower panels). Scale bars adjacent to heat maps indicate linear fold change (control (C) set to 1). E. Expression of *SIRT5*, *MITF* and the *MITF* target, *PPARGC1A* are positively correlated in melanoma clinical samples ($p<0.0001$, data from TCGA, analyzed on cBioPortal; see Figure 1A).

Figure 7

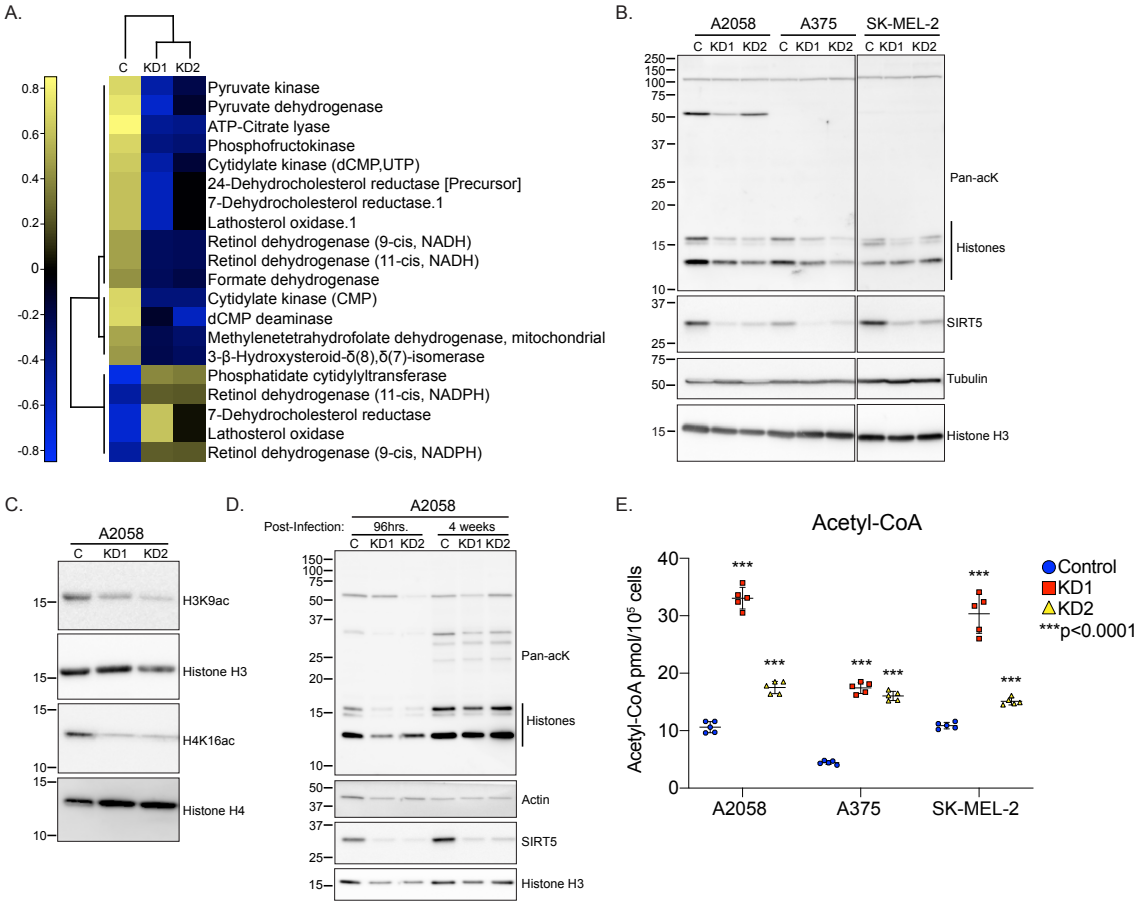

Figure 7 SIRT5 promotes histone acetylation in melanoma.
A. Heatmap of z-scores calculated from metabolic reaction fluxes predicted by genome-scale modeling to be differentially active ($p<0.01$) after SIRT5 KD. B. Total histone acetylation is reduced 96 hrs. post-transduction with shRNAs targeting SIRT5 (KD1 or KD2) compared to a non-targeting control (C) in melanoma cell lines. C. Immunoblot demonstrating loss of H3K9ac and H4K16ac 96 hrs. post-transduction with shRNAs targeting *SIRT5* (KD1 or KD2) compared to a non-targeting control (C) in A2058 cells. D. Acetylation is restored in A2058 cells lacking SIRT5 after 4 weeks of continual culture in puromycin. E. Total cellular acetyl-CoA levels are increased in A2058, A375 and SK-MEL-2 cells 96 hrs. after SIRT5 depletion. Acetyl-CoA abundance was quantified by liquid chromatography-high resolution mass spectrometry and normalized to cell number. Plotted are average (n=5) acetyl-CoA levels as pmol acetyl-CoA/10^5 cells. Error bars represent SD.

Figure 8

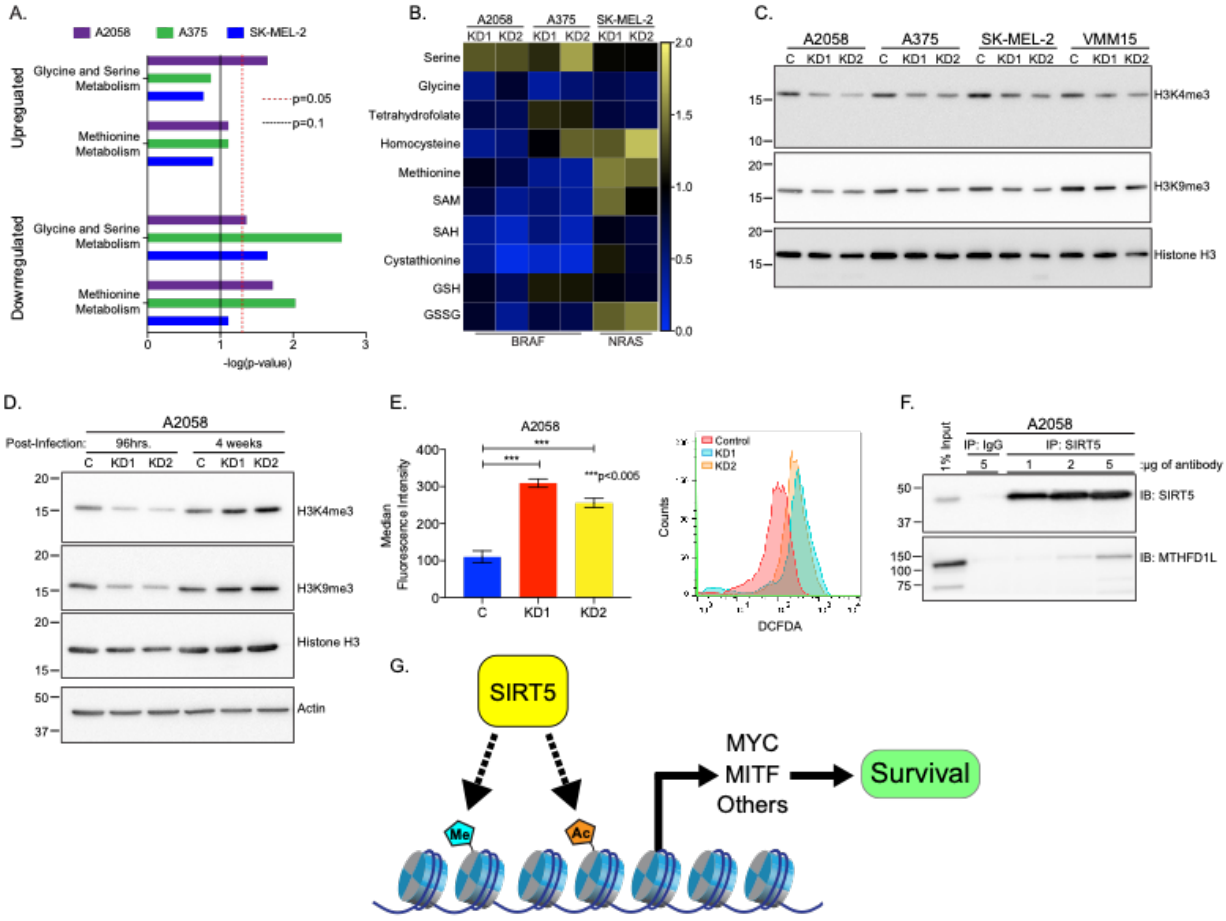

Figure 8 SIRT5 promotes histone methylation and reduced cellular ROS levels in melanoma.
A. LC-MS/MS-based metabolite profiling followed by MetaboAnalyst pathway analysis demonstrate alterations in glycine and serine and methionine biosynthesis pathways in melanoma cells upon SIRT5 depletion. B. Perturbations in 1C metabolite levels in response to SIRT5 loss in the cell lines shown. Each column represents the mean of 3 independently prepared biological replicates. Metabolite levels in SIRT5 depleted (KD1 and KD2, as indicated) samples are normalized to control. SAM, S-adenosyl-methionine; SAH, S-adenosylhomocysteine; GSH, reduced glutathione; GSSG, glutathione disulfide. C. H3K4me3 and H3K9me3 immunoblot in melanoma cells 96 hrs. post-transduction with shRNAs targeting *SIRT5* (KD1 or KD2) compared to a non-targeting control (C). D. H3K4me3 and H3K9me3 levels are restored in A2058 cells lacking SIRT5 after 4 weeks of continual culture in puromycin. E. Flow cytometric analysis of DCFDA-stained A2058 cells 96 hrs. post-transduction with shRNAs targeting SIRT5 (KD1 or KD2) reveals increased ROS compared to a non-targeting control (C), $p<0.005$. Left panel, average mean fluorescence intensity of DCFDA positive populations in n=3 samples. Error bars represent SD. Right panel, representative flow cytometric of A2058 cells stained with DCFDA. F. SIRT5 interacts with MTHFD1L in A2058 cells. Increasing amounts of anti-SIRT5 antibody increases SIRT5-MTHFD1L coprecipitation compared to normal rabbit IgG control. Basal expression of SIRT5 and MTHFD1L in whole-cell extract (1% of initial amount used for immunoprecipitation) is shown for comparison. G. Proposed model of promotion of MITF and c-MYC expression via SIRT5-dependent chromatin modifications in human melanoma. Me, methylation; Ac, acetylation.